

Comparative analysis of machine learning methods for active flow control

Fabio Pino¹†, Lorenzo Schena¹, Jean Rabault²,
Alexander Kuhnle³, and Miguel A. Mendez¹

¹von Karman Institute for Fluid Dynamics, EA Department, Sint Genesius Rode, Belgium

²Norwegian Meteorological Institute, Oslo, Norway

³Dep. of Computer Science and Technology, University of Cambridge, Cambridge, UK

Machine learning frameworks such as Genetic Programming (GP) and Reinforcement Learning (RL) are gaining popularity in flow control. This work presents a comparative analysis of the two, bench-marking some of their most representative algorithms against global optimization techniques such as Bayesian Optimization (BO) and Lipschitz global optimization (LIPO). First, we review the general framework of the flow control problem, linking optimal control theory with model-free machine learning methods. Then, we test the control algorithms on three test cases. These are (1) the stabilization of a nonlinear dynamical system featuring frequency cross-talk, (2) the wave cancellation from a Burgers' flow and (3) the drag reduction in a cylinder wake flow. Although the control of these problems has been tackled in the recent literature with one method or the other, we present a comprehensive comparison to illustrate their differences in exploration versus exploitation and their balance between 'model capacity' in the control law definition versus 'required complexity'. We believe that such a comparison opens the path towards hybridization of the various methods, and we offer some perspective on their future development in the literature of flow control problems.

Key words: Optimal Flow control and Machine Learning, Bayesian Optimization, LIPO Optimization, Genetic Programming, Reinforcement Learning

1. Introduction

The multidisciplinary nature of active flow control has attracted interests from many research areas for a long time (Gunzburger 2002; Wang & Feng 2018; el Hak 2000; Bewley 2001) and its scientific and technological relevance have ever growing proportions (Brunton & Noack 2015; Noack *et al.* 2022; Bewley 2001). Indeed, the ability to interact and manipulate a fluid system to improve its engineering benefits is essential in countless problems and applications, including laminar to turbulent transition (Schlichting Deceased; Lin 2002), drag reduction (el Hak 2000; Wang & Feng 2018), stability of combustion systems (Lang *et al.* 1987), flight mechanics (Longuski *et al.* 2014), wind energy (Apata & Oyedokun 2020; Munters & Meyers 2018), and aeroacoustic noise control (Collis *et al.* 2002; Kim *et al.* 2014), to name just a few.

The continuous development of computational and experimental tools, together with the advent of data-driven methods from the ongoing machine learning revolution, are reshaping tools and methods in the field (Noack *et al.* 2022; Noack 2019). Nevertheless, the quest for reconciling terminology and methods from the machine learning and the control theory community has a long history (see Bersini & Gorrini (1996) and Sutton *et al.* (1992)) and it is still ongoing, as described

† Email address for correspondence: fabio.pino@vki.ac.be

in the recent review by [Recht \(2019\)](#) and [Nian *et al.* \(2020\)](#). This article aims at reviewing some recent machine learning algorithms for flow control, presenting a unified framework that highlights differences and similarities amidst various techniques. We hope that such a generalization opens the path towards hybrid approaches.

In its most abstract formulation, the (flow) control problem is essentially a functional optimization problem constrained by the (fluid) systems' dynamics ([Stengel 1994](#); [Kirk 2004](#)). As further discussed in Section 2, the goal is to find a control function that minimizes (or maximizes) a cost (or reward) functional which measures the controller performances (e.g. drag or noise reduction). Following Wiener's metaphors ([Wiener 1948](#)), active control methods can be classified as white, grey or black depending on how much knowledge about the system is used to solve the optimization: the whiter the approach, the more the control relies on the analytical description of the system to be controlled.

In a white box method, the equations governing the system to be controlled are known and amenable to analytical treatment. This enables tools from optimal control theory such as Pontryagin's principle or the Hamilton-Jacobi-Bellman optimality condition ([Stengel 1994](#); [Kirk 2004](#)). The literature of optimal control theory further classifies a control technique as direct or indirect ([Rao 2009](#); [Biral *et al.* 2016](#)) depending on whether the necessary conditions for optimality is used in its continuous form. Leveraging on the analytical description of the system, calculus of variation and Pontryagin's principle, these conditions render as a set of differential equations with given initial and final conditions, i.e. a two-point boundary value problem (TPBVP). Indirect methods exploit this TPBVP in various ways, either by seeking a numerical solution via shooting or collocation methods or to compute gradients of the cost function with respect to the control parameters, as in adjoint-based optimal control ([Carnarius *et al.* 2010](#); [Bewley *et al.* 2001](#); [Kim *et al.* 2014](#); [Delport *et al.* 2011](#); [Nita *et al.* 2016](#); [Meliga *et al.* 2010](#); [Flinois & Colonius 2015](#)). Direct methods ([Böhme & Frank 2017](#)) translate the optimal control problem into a discrete constrained optimization or nonlinear programming problem ([Kraft 1985](#); [Bazaraa *et al.* 2005](#)).

Significant simplifications are possible if three conditions are met: (1) the system is linear (2) the control law to be derived is linear with respect to the state and (3) the performance measure is quadratic. In this case, the principles of optimal control lead to the well known Linear Quadratic Regulator (LQR) ([Stengel 1994](#); [Kim & Bewley 2007](#); [Sipp & Schmid 2016](#)) and the optimal control law is analytically available. The LQR is arguably the most common tool also for nonlinear systems, provided that these are close enough to a fixed point around which the controller seeks to keep the system. An extensive literature review of linear control theory for fluid flows is provided by [Brunton & Noack \(2015\)](#). Tools from linear control theory have often been combined with tools from system identification ([Brunton 2022](#)), which seeks to identify the best linear model for a dynamical system by using input-output data ([Proctor *et al.* 2016](#); [Brunton 2009](#); [Rowley 2005](#)). These approaches are "grey", in the sense that a "surrogate" model is used to derive the optimal control law.

Within the direct methods, a radically different perspective –central to this work– is provided by "black-box" or "model-free" methods. In these approaches, only input-output relations are used in the search for the optimal control law. This is a radical change of paradigm compared with the analytical-based control strategies such as the adjoint method, as knowledge of the system is gathered by only interacting with it. The popularity of these heuristic approaches has been growing considerably in the last decade, promoted by the popularization of machine learning tools, the development of new algorithms, and the increase in available computational power.

Machine learning ([Abu-Mostafa *et al.* 2012](#); [Mitchell 1997](#); [Vladimir Cherkassky 2008](#); [Brunton *et al.* 2020](#)) is a subset of Artificial Intelligence which combines optimization and statistics to "learn" (i.e. calibrate) models from data (i.e. experience). These models can be general enough to describe any (nonlinear) function without requiring prior knowledge and can be encoded in various

forms: examples are parametric models such as Radial Basis Function (RBFs, see [Fasshauer \(2007\)](#)) expansions or Artificial Neural Networks (ANNs, see [Goodfellow et al. \(2016\)](#)), or tree structures of analytic expressions such as in Genetic Programming (GP [Koza \(1994\)](#)). The process by which these models are "fitted" to (or "learned" from) data is an optimization in one of its many forms ([Sun et al. 2019](#)): continuous or discrete, global or local, stochastic or deterministic. Within the flow control literature, at the time of writing, the two most prominent model-free control techniques from the machine learning literature are Genetic Programming ([Koza 1994](#)) and Reinforcement Learning ([Sutton & Barto 2018](#)). Both are reviewed in this article.

Genetic Programming (GP) is an evolutionary computational technique developed by [Koza \(1994\)](#) as a new paradigm for automatic programming and machine learning ([Banzhaf et al. 1997](#); [Vanneschi & Poli 2012](#)). GP optimizes both the structure and the parameters of a model, which is usually constructed as recursive trees of predefined functions connected through mathematical operations. The use of GP for flow control has been pioneered and popularized by [Noack and coworkers \(Noack 2019; Duriez et al. 2017\)](#). Successful examples on experimental problems include the drag reduction past bluff bodies ([Li et al. 2017](#)), shear flow separation control ([Gautier et al. 2015](#); [Debien et al. 2016](#); [Benard et al. 2016](#)) and many more, as reviewed by [Noack \(2019\)](#). More recent extensions of this "Machine Learning Control" (MLC) approach, combining genetic algorithms with the down-hill simplex method, have been proposed by [Li et al. \(2019\)](#) and [Maceda et al. \(2021\)](#).

Reinforcement Learning (RL) is one of the three main machine learning paradigms and encompasses learning algorithms collecting data "online", in a trial and error process. In Deep RL (DRL), the control law (known as policy) is modelled by an ANN which needs to be trained. The use of an ANN to parametrize control laws has a long history (see [Lee et al. \(1997\)](#)), but their application to flow control, leveraging on RL algorithms, is at its infancy (see also [Li & Zhang \(2021\)](#) for a recent review). The landscape of RL is vast and grows at a remarkable pace, fostered by the recent success in strategy board games ([Silver et al. 2016, 2018](#)), video games ([Szita 2012](#)), robotics ([Kober & Peters 2014](#)), language processing ([Luketina et al. \(2019\)](#)) and more. In the literature of flow control, RL has been pioneered by [Komoutsakos and coworkers \(Gazzola et al. 2014; Verma et al. 2018\)](#) (see also [Garnier et al. \(2021\)](#) and [Rabault & Kuhnle \(2022\)](#) for more literature). The first applications of RL in fluid mechanics were focused on the study of collective behavior of swimmers ([Wang & Feng 2018](#); [Verma et al. 2018](#); [Novati et al. 2017](#); [Novati & Koumoutsakos 2019](#); [Novati et al. 2019](#)), while the first applications for flow control were presented by [Pivot et al. \(2017\)](#) and by [Rabault et al. \(2019, 2020\)](#); [Rabault & Kuhnle \(2019\)](#). A similar flow control problem has been solved numerically and experimentally via RL by [Fan et al. \(2020\)](#). [Bucci et al. \(2019\)](#) showcased the use of RL to control chaotic systems such as the one-dimensional Kuramoto–Sivashinsky equation; [Beintema et al. \(2020\)](#) used it to control heat transport in a two-dimensional Rayleigh–Bénard systems while [Belus et al. \(2019\)](#) used RL to control the interface of unsteady liquid films. Ongoing efforts in the use of DRL for flow control are focused with increasing the complexity and nonlinearity of the problems treated, either by increasing the Reynolds number (see [Ren et al. \(2021\)](#)), or by considering more challenging and realistic configurations ([Vinueza et al. 2022](#)).

In this article, we consider the Deep Deterministic Policy Gradient (DDPG) ([Lillicrap et al. 2015](#)) as a representative deterministic RL algorithm. This is introduced in Section 3.3, and the results obtained for one of the investigated test cases are compared with those obtained by [Tang et al. \(2020\)](#) using a stochastic RL approach, namely the Proximal Policy Optimization (PPO) ([Schulman et al. \(2017\)](#)). It is worth noticing that the boundaries between GP and RL are more methodological than conceptual: as highlighted by [Banzhaf et al. \(1997\)](#), many fitness functions in GP can lead to RL systems. Yet, GP and RL are often presented as different frameworks.

This work puts GP and RL in a global control framework and benchmarks their performances against simpler black-box optimization methods. Within this category, we include model-free

control methods in which the control action is predefined and prescribed by a few parameters (e.g. a simple linear controller), and the model learning is driven by global black-box optimization. This approach, using Genetic Algorithms, has a long history (Fleming & Fonseca 1993). However, we here focus on more sample efficient alternatives: the Bayesian Optimization (BO) and the Lipschitz global Optimization technique (LIPO). Both are described in Section 3.1.

The BO is arguably the most popular "surrogate-based", derivative-free, global optimization tool, popularized by Jones *et al.* (1998) and their Efficient Global Optimization (EGO) algorithm. In its most classic form (Forrester *et al.* 2008; Archetti & Candelieri 2019), the BO uses a Gaussian process (Rasmussen & Williams 2005) for regression of the cost function under evaluation and an acquisition function to decide where to sample next. This method has been used by Mahfoze *et al.* (2019) for reducing the skin-friction drag in a turbulent boundary layer and by Blanchard *et al.* (2022) for reducing the drag in the fluidic pinball and for enhancing mixing in a turbulent jet.

The LIPO algorithm is a more recent global optimization strategy proposed by Malherbe & Vayatis (2017). This is a sequential procedure to optimize a function under the only assumption that it has a finite Lipschitz constant. Since this method has virtually no hyper-parameters involved, variants of the LIPO are becoming increasingly popular in hyper-parameter calibration of machine learning algorithms (Ahmed *et al.* 2020), but to the authors' knowledge it has never been tested on flow control applications.

All of the aforementioned algorithms are analyzed on three test cases of different dimensions and complexity. The first test case is the 0D model proposed by Duriez *et al.* (2017) as the simplest dynamical system reproducing the frequency cross-talk encountered in many turbulent flows. The second test case is the control of nonlinear travelling waves described by the 1D Burgers' equation. This test case is representative of the challenges involved in the control of advection-diffusion problems. Moreover, recent works on Koopman analysis by Page & Kerswell (2018) and Balabane *et al.* (2021) have provided a complete analytical linear decomposition of the Burgers' flow and might render this test case well suited to test the full arsenal of possible "white-box" control methods. Finally, the last selected test case is arguably the most well known benchmark in flow control: the drag attenuation in the flow past a cylinder. This problem has been tackled by nearly the full spectra of control methods in the literature, including reduced order models and linear control (Seidel *et al.* 2008; Bergmann *et al.* 2005; Park *et al.* 1994), resolvent-based feedback control (Jin *et al.* 2020), reinforcement learning via stochastic (Rabault *et al.* 2019) and deterministic algorithms (Fan *et al.* 2020), and reinforcement learning assisted by stability analysis (Li *et al.* 2017).

In the literature on machine learning methods for flow control, both the first and the last test cases have been tackled by either GP or RL. We here benchmark both methods on the same test cases against classic black-box optimization. Emphasis is given to the different precautions these algorithms require, the number of necessary interactions with the environment, the different approaches to balance exploration and exploitation, and the differences (or similarities) in the derived control laws. The remaining of the article is structured as follows. Section 2 recalls the conceptual transition from optimal control theory to machine learning control. Section 3 briefly recalls the machine learning algorithm analyzed in this work, while Section 4 describes the introduced test cases. Results are collected in Section 5 while conclusions and outlooks are given in Section 6.

2. From optimal control to machine learning

This section briefly presents the framework linking optimal control, reinforcement learning and global optimization methods. We refer the reader the literature (Sutton & Barto 2018; Evans 1983; Stengel 1994; Kirk 2004) for more details. We introduce the optimal control problem in 2.1 and we focus on model-free learning based control in 2.2.

2.1. Methods from Optimal Control Theory

An optimal control problem consists in finding a *control action* $\mathbf{a}(t)$, within a feasible set \mathcal{A} , which optimizes a functional measuring our ability to keep a flow (*plant* in control theory and *environment* in reinforcement learning) close to the desired states or conditions. The functional is usually a cost to minimize in control theory and a payoff to maximize in reinforcement learning. We focus on the second and denote the reward function as $R(\mathbf{a})$. The optimization is constrained by the plant/environment's dynamic:

$$\begin{aligned} \max_{\mathbf{a}(t) \in \mathcal{A}} \quad & R(\mathbf{a}) = \phi(\mathbf{s}(T)) + \int_0^T \mathcal{L}(\mathbf{s}(\tau), \mathbf{a}(\tau), \tau) d\tau, \\ \text{s.t.} \quad & \begin{cases} \dot{\mathbf{s}}(t) = \mathbf{f}(\mathbf{s}(t), \mathbf{a}(t), t) & t \in (0, T] \\ \mathbf{s}(0) = \mathbf{s}_0 \end{cases}, \end{aligned} \quad (2.1)$$

where $\mathbf{f}: \mathbb{R}^{n_s} \times \mathbb{R}^{n_a} \rightarrow \mathbb{R}^{n_s}$ is the vector field in the phase space of the dynamical system, $\mathbf{s} \in \mathbb{R}^{n_s}$ is the system's *state* vector evolving along a *trajectory*, $\mathbf{a} \in \mathbb{R}^{n_a}$ is the action/actuation, taken by a *controller* in control theory and an *agent* in reinforcement learning.

The functional $R(\mathbf{a})$ comprises a *running cost* (or Lagrangian) $\mathcal{L}: \mathbb{R}^{n_a} \times \mathbb{R}^{n_s} \rightarrow \mathbb{R}$, which accounts for the system's states evolution, and a *terminal cost* (or Mayer term) $\phi: \mathbb{R}^{n_s} \rightarrow \mathbb{R}$, which depends on the final state condition. Optimal control problems with this cost functional form are known as Bolza problem (Stengel 1994; Evans 1983; Kirk 2004).

The agent/controller selects the action/actuation from a *control law* or *policy* $\pi: \mathbb{R}^{n_s} \rightarrow \mathbb{R}^{n_a}$:

$$\mathbf{a}(t) = \pi(\mathbf{s}(t), t) \in \mathbb{R}^{n_a}. \quad (2.2)$$

Note that the system might not be fully observable, and hence the policy would generally depend on some observation $\mathbf{y} = O(\mathbf{s}(t)) \in \mathbb{R}^{n_o}$, with $n_o \ll n_s$. However, as we later focus on black-box methods, this clarification is unessential.

Identifying the best policy $\mathbf{a}^*(t) = \pi^*(\mathbf{s}(t), t)$ is the goal of optimal control theory and reinforcement learning alike. When the agent/controller acts according to π^* , the state evolves along the optimal trajectory $\mathbf{s}^*(t)$. Using calculus of variation, the necessary condition for optimality is the minimum of the augmented reward functional $R_A(\mathbf{a})$ which adjoints the equality constraint $\dot{\mathbf{s}}(t) - \mathbf{f}(\mathbf{s}(t), \mathbf{a}(t), t) = 0$ using a vector of Lagrangian multipliers $\lambda \in \mathbb{R}^n$:

$$R_A(\mathbf{a}) = R(\mathbf{a}) + \lambda^T [\dot{\mathbf{s}}(t) - \mathbf{f}(\mathbf{s}(t), \mathbf{a}(t), t)]. \quad (2.3)$$

The vector $\lambda \in \mathbb{R}^n$ is also known as the *adjoint vector* or *costate* and represent the cost sensitivity to perturbation of the trajectory $\mathbf{s}(t)$, i.e $\lambda = -\partial_{\mathbf{s}} \mathcal{H}(\mathbf{s}, \mathbf{a}(t), \lambda(t))^T$.

It can be shown (Stengel 1994; Kirk 2004; Evans 1983) that the optimal control law/policy is the one that maximizes the *Hamiltonian* $\mathcal{H}(\mathbf{s}, \mathbf{a}(t), \lambda(t))$ of the system, defined as:

$$\mathcal{H} := \mathcal{L}(\mathbf{s}(t), \mathbf{a}(t), t) + \lambda(t)^T (\dot{\mathbf{s}}(t) - \mathbf{f}(\mathbf{s}(t), \mathbf{a}(t), t)), \quad (2.4)$$

i.e.:

$$\mathbf{a}^*(t) = \arg \max_{\mathbf{a} \in \mathcal{A}} \{ \mathcal{H}(\mathbf{s}, \mathbf{a}, \lambda(t)) \}. \quad (2.5)$$

The costate vector in the Hamiltonian satisfies the following system of ordinary differential equations:

$$\begin{cases} \dot{\lambda}(t) = -\partial_{\mathbf{s}} \mathbf{f}^T \lambda(t) - \partial_{\mathbf{s}} \mathcal{L}(\mathbf{s}, \mathbf{a}(t), t)^T & t \in (0, T] \\ \lambda(T) = \partial_{\mathbf{s}} \phi(\mathbf{s}(T))^T \end{cases}, \quad (2.6)$$

having used the short hand notation ∂_x for the partial derivatives $\partial/\partial x$, so that $\partial_{\mathbf{s}} \mathcal{L}$ is the gradient of the Lagrangian over the action vector and $\partial_{\mathbf{s}} \mathbf{f}$ is the Jacobian of the dynamical system's flow. Equation (2.5), together with (2.6), state the Pontryagin principle (Stengel 1994; Evans 1983; Kirk 2004). This defines the necessary condition for optimality of the control law/policy and is the backbone of adjoint-based control methods.

More specifically, the gradient $\partial_{\mathbf{a}} \mathcal{L}$ and the Jacobian $\partial_{\mathbf{s}} \mathbf{f}$ can be computed once the system and the cost function are defined. Then, the system (2.6) can be integrated backward in time from the terminal state $\lambda(T)$ for any 'tentative' control action $\mathbf{a}(t)$. Given $\mathbf{a}(t)$ and $\lambda(t)$, it is possible to compute the gradient of the Hamiltonian with respect to the control action:

$$\partial_{\mathbf{a}} \mathcal{H}(\mathbf{s}, \mathbf{a}, \lambda) = \partial_{\mathbf{a}} \mathcal{L}(\mathbf{s}(t), \mathbf{a}(t), t) + \lambda^T \partial_{\mathbf{a}} \mathbf{f}(\mathbf{s}(t), \mathbf{a}(t), t). \quad (2.7)$$

This information can then be used to improve the selected action in a gradient-based manner. For example, assuming that the action is given by a parametric form $\mathbf{a} = \pi(\mathbf{s}; \mathbf{w})$, depending on a set of weights $\mathbf{w} \in \mathbb{R}^{n_w}$, an adjoint-based gradient ascent step can be

$$\mathbf{w} \leftarrow \mathbf{w} + \alpha \partial_{\mathbf{w}} \mathcal{H}(\mathbf{s}, \mathbf{a}(\mathbf{w}), \lambda), \quad (2.8)$$

with $\alpha \in \mathbb{R}$ a suitable learning rate and $\partial_{\mathbf{w}} \mathcal{H} = \partial_{\mathbf{a}} \mathcal{H} \partial_{\mathbf{w}} \mathbf{a}$ the gradient of the Hamiltonian with respect to the weights. Having access to the analytic evaluation of the cost function's gradient enable also more sophisticated Quasi-Newton methods (see for instance Nita *et al.* (2016)). The power of adjoint-based control is in its independence from the control vector dimension n_a or the number of parameters n_w : for an actuation law $\mathbf{a}(t)$, the cost to evaluate the gradient $\partial_{\mathbf{a}} \mathcal{H}$ is the cost of one 'forward' integration of the system to evaluate the states $\mathbf{s}(t)$ plus one 'backward' integration of the ODE (2.6) to evaluate the costate $\lambda(t)$.

A different approach, providing both a necessary and sufficient condition for optimality, is dynamic programming. This approach is based on the definition of a *value function* which measures the quality of a given state $\mathbf{s}(t)$ according to a policy $\pi(\mathbf{s})$ in (2.2). In other terms, this function gives the minimal cost/maximum reward achievable by a controller/agent following π , from $\mathbf{s}(t)$ to $\mathbf{s}(T)$:

$$V^\pi(t, \mathbf{s}(t)) = \phi(\mathbf{s}(T)) + \int_t^T \mathcal{L}(\mathbf{s}(t), \mathbf{a}(t), t) dt. \quad (2.9)$$

The central result in dynamic programming is that the optimal policy π^* , namely the one leading to $V^* := V^{\pi^*} = \sup V^\pi$ for all states, satisfies the Hamilton–Jacobi–Bellman (HJB) partial differential equation:

$$\partial_t V^*(\mathbf{s}, t) + \max_{\mathbf{a} \in \mathcal{A}} \left\{ \mathcal{L}(\mathbf{s}, \mathbf{a}, t) + \partial_{\mathbf{s}} V^*(\mathbf{s}, t) \mathbf{f}(\mathbf{s}, \mathbf{a}, t) \right\} = 0, \quad (2.10)$$

starting from the terminal condition $V^*(T) = \phi_r(T)$.

After solving the HJB and hence obtaining the optimal value function, the optimal policy is found indirectly as the result of a maximization process:

$$\mathbf{a}^*(t) = \arg \max_{\mathbf{a} \in \mathcal{A}} \left\{ \mathcal{L}(\mathbf{s}, \mathbf{a}, t) + \partial_{\mathbf{s}} V^*(\mathbf{s}, t) \mathbf{f}(\mathbf{s}, \mathbf{a}, t) \right\}. \quad (2.11)$$

Besides the difficulties in solving the HJB, the main problem of this approach is that every time step requires an expensive maximization to define the best action. Moreover, the numerical integration of (2.10) requires the discretization of the state space, which scales exponentially with n_s . This limit is known as the curse of dimensionality and prevents the application of dynamic programming to many flow control problems of interest even if the dynamical system is analytically tractable and its states are fully observable. The tools presented in this section provides the foundation to the model-free approaches discussed next.

2.2. Model Free Control and Machine Learning

In the context of machine learning control, the equations governing the system are unknown, and the controller is designed relying only on input/output relations. As shown in Figure 1, the dynamics of the system $\mathbf{f}(\mathbf{s}, \mathbf{a}, t)$, as well as the performance measures $R(\mathbf{a})$, are embedded into an unknown “black-box function” and the algorithm looks for an optimal control/policy through an iterative trial and error process.

We uniformly discretize the time interval $t \in [0, T]$ in (2.1) as $t_k = k\Delta t$, leading to $N = T/\Delta t + 1$ points indexed as $k = 0, \dots, N-1$ and we introduce the notation $\mathbf{s}_k = \mathbf{s}(t_k)$. Although it is impossible to predict the response of the system to an action, i.e. $\mathbf{s}_{k+1} = \mathbf{f}(\mathbf{s}_k, \mathbf{a}_k^\pi, k)$, it is possible to collect a sequence of states $\mathbf{S} := \{\mathbf{s}_1, \mathbf{s}_2 \dots \mathbf{s}_N\}$ while taking a sequence of actions $\mathbf{A}^\pi := \{\mathbf{a}_1, \mathbf{a}_2 \dots \mathbf{a}_N\}$. Moreover, one reward with $\mathcal{L}(\mathbf{s}_k, \mathbf{a}_k, k)$ each state-action pair as a function of time (index). In an episodic approach, each set of N interactions with the system is an *episode*, at the end of which it is possible to compute a discrete version of the performance measures $R(\mathbf{a})$ in (2.1):

$$R(\mathbf{A}^\pi) = \phi(\mathbf{s}_N) + \sum_{k=0}^{N-1} \mathcal{L}(\mathbf{s}_k, \mathbf{a}_k^\pi, k). \quad (2.12)$$

In the RL literature, this is known as cumulative reward and the Lagrangian takes the form $\mathcal{L}(\mathbf{s}_k, \mathbf{a}_k^\pi, k) = \gamma^k r(\mathbf{s}_k, \mathbf{a}_k^\pi) = \gamma^k r_k^\pi$, where $\gamma \in [0, 1]$ is a discount factor which prioritize immediate over future rewards. In a deterministic policy, the sequence of actions is taken from a parametric function which we denote $\mathbf{a}^\pi = \pi(\mathbf{s}; \mathbf{w})$. In a stochastic policy, the parametric function outputs the parameters of the distribution (e.g mean and standard deviation in a Gaussian) from which the actions will be sampled. In both cases, the vector $\mathbf{w} \in \mathbb{R}^{l_w}$ is unknown and must be *learned*. By mapping the action space \mathcal{A} onto a finite weight space $\mathbf{w} \in \mathbb{R}^{l_w}$, the variational problem of maximizing $R(\mathbf{a}(t))$ reduces to the optimization problem of maximizing $R(\mathbf{w})$.

A machine learning-based controller (see Figure 1) is thus an optimizer of $R(\mathbf{w})$ which proceeds iteratively while interacting with the environment. At every iteration n , the update \mathbf{w}_{n+1} hopefully leads to better performances than the previous, i.e. $R(\mathbf{w}_n) < R(\mathbf{w}_{n+1})$. Although there is no guarantee that the optimal control law/policy can be found, and we have no means to attack neither (2.7) nor (2.10), it is possible to give a value to a state \mathbf{s} under the policy π and hence have the discrete version of (2.9):

$$\mathbf{V}^\pi(\mathbf{s}_t) = \phi(\mathbf{s}_N) + \sum_{k=t}^N \mathcal{L}_r(\mathbf{s}_k, \mathbf{a}_k^\pi, k) = \phi(\mathbf{s}_N) + \sum_{k=t}^N \gamma^{k-t} r_k = r_k + \gamma \mathbf{V}^\pi(\mathbf{s}_{t+1}). \quad (2.13)$$

One thus has $R(\mathbf{A}^\pi) = \mathbf{V}^\pi(\mathbf{s}_1)$. Moreover, one might occasionally let the environment/controller act *off-policy* and thus take an action \mathbf{a}_k rather than \mathbf{a}_k^π . Then, it is worth defining the value of a state-action pair $(\mathbf{s}_t, \mathbf{a}_t)$ under policy π as:

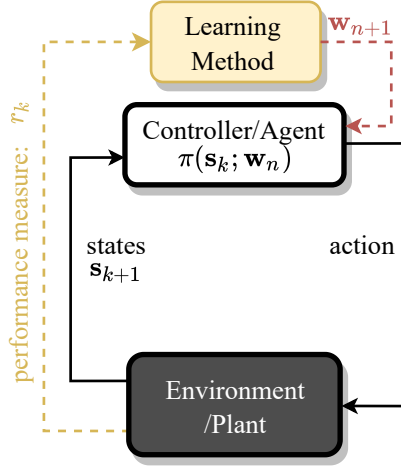


Figure 1: General setting for a machine learning-based control problem: the learning algorithm improves the agent/control performances by interacting with the environment/plant. The agent/controller acts according to a parametric law and receives a feedback on its actions. The control problem is an optimization of the weights to maximize a function of actions and states.

$$\begin{aligned} \mathbf{Q}^\pi(\mathbf{s}_t, \mathbf{a}_t) &= \phi_r(\mathbf{s}_N) + r(\mathbf{s}_k, \mathbf{a}_k) + \sum_{k=t+1}^N \mathcal{L}_r(\mathbf{s}_k, \mathbf{a}_k^\pi, k) \\ &= r(\mathbf{s}_k, \mathbf{a}_k) + \gamma \mathbf{V}^\pi(\mathbf{s}_{t+1}). \end{aligned} \quad (2.14)$$

This function, known as Q -function, measures the reward that can be obtained if a ‘de-tour’ from the current policy is taken at time k , the action \mathbf{a}_k is taken instead of \mathbf{a}_k^π , and the policy π is followed *afterwards*. It is therefore possible to define the *advantage* of such exploration as

$$\mathbf{A}^\pi(\mathbf{s}_t, \mathbf{a}_t) = r(\mathbf{s}_t, \mathbf{a}_t) - r(\mathbf{s}_k, \mathbf{a}_k^\pi) = \mathbf{Q}^\pi(\mathbf{s}_t, \mathbf{a}_t) - \mathbf{V}^\pi(\mathbf{s}_t). \quad (2.15)$$

If the optimal policy is followed, the advantage is zero. It is worth noticing that all the definitions (2.13), (2.14), (2.15) assume that the system is deterministic. This is uncommon in the literature of RL, where the environment is usually treated as stochastic and modelled as a Markov Decision Process (MDP) (Sutton & Barto 2018). We briefly reconsider the stochastic approach in the description of the DDPG in section 3.3. For a deterministic system, one has

$$R(\mathbf{w}) = V^\pi(\mathbf{s}_0) = Q(\mathbf{s}_0, \mathbf{a}_0^\pi). \quad (2.16)$$

Control methods based on machine learning differ in the form of the policy parametrization $\mathbf{a} = \pi(\mathbf{s}_t, \mathbf{w})$, and the use of data and function approximators to compensate for the lack of solid theoretical tools such as (2.4) and (2.11).

Some machine learning tools ‘imitates’ (2.4) and –borrowing from the RL literature– could be classified as *actor-only*. These methods focus on the policy parametrization and seek to maximize $R(\mathbf{A}(\mathbf{w}))$ regardless of the physical constraints $\dot{\mathbf{s}}(t) - \mathbf{f}(\mathbf{s}(t), \mathbf{a}(t), t) = 0$ in (2.1), or, in a sense, taking $\lambda = \mathbf{0}$ in (2.3). Actor-only methods are essentially optimizers coupled with a (possibly adaptive) policy parametrization. Like all optimizers, these can be global and gradient-free or local and gradient-based, and might use surrogate functions to approximate the function $R(\mathbf{w})$. Within this last category, we consider the BO and LIPO in section 3.1. Among the gradient-free, actor-only methods, the most classic approach is the GP, briefly described in Section 3.2.

The main difference between black box optimization and reinforcement learning is that the second seeks to approximate the value function Q in (2.16). The interest in such approximation depends on whether the algorithm is *actor-only* or *critic-only*. An *actor-only* RL approach focuses on learning $Q(s_t, \mathbf{a}_t)$ to enable the computation of the gradient $\partial_w R = \partial_a Q \partial_w \mathbf{a}$. This can then be used for gradient based optimization. The most classic example of this category is REINFORCE (Williams 1992; Sutton & Barto 2018). A *critic-only* RL focuses on learning $Q(s_t, \mathbf{a}_t)$ to then take actions such that $\mathbf{a}_t = \arg \max_{\mathbf{a} \in \mathcal{A}} Q^\pi(s, \mathbf{a})$. The most classic example of this category, also known as ‘off-policy’ methods, is deep Q learning (Mnih *et al.* 2013). Modern RL algorithms are actor-critic, i.e. combine both approaches. The DDPG algorithm implemented in this work falls within this category and is described in Section 3.3.

3. Implemented Algorithms

3.1. Optimization via BO and LIPO

Let the policy be described by a predefined function $\mathbf{a} = \pi(s_t, \mathbf{w}^\pi) \in \mathbb{R}^{n_a}$, defined by a set of weights $\mathbf{w}^\pi \in \mathcal{W} \subseteq \mathbb{R}^{n_w}$. This function could be a linear mapping, a user-defined nonlinear function, or any other parametric model from machine learning (r.g. RBFs or ANNs). We assume in this section that this model depends on a relatively small number of parameters (say $n_w \sim \mathcal{O}(10)$). For a given set of weights, the policy defines the behaviour of the agent/controller and the cumulative reward at each episode can be computed from (2.12). In a stochastic system, the cumulative reward varies even if the same set of weights is considered: in this case, we shall repeat the evaluation of a set of weights multiple times and average the results. In both cases, the problem is now an optimization, in which every episode gives an evaluation of a "black-box" function $R(\mathbf{w})$ (or its expectation over a number of episodes). Because this function might be expensive, we focus on efficient optimizers. Other methods are illustrated by Maceda *et al.* (2018).

3.1.1. Bayesian Optimization (BO)

The first ingredient of BO is a regression tool that derives a surrogate model of the function to optimize. Among several options, the classic BO uses a Gaussian Process (GPr) as surrogate function. Let $\mathbf{W}^* := \{\mathbf{w}_1, \mathbf{w}_2 \dots \mathbf{w}_{n_*}\}$ be a set of n_* tested weights and $\mathbf{R}^* := \{R_1, R_2 \dots R_{n_*}\}$ the associated cumulative rewards. The GPr offers a probabilistic model that computes the probability of a certain reward given the observations $(\mathbf{W}^*, \mathbf{R}^*)$, i.e. $p(R(\mathbf{w})|\mathbf{W}^*, \mathbf{R}^*)$. In a GPr, this is

$$p(R(\mathbf{w})|\mathbf{R}^*, \mathbf{W}^*) = \mathcal{N}(\mu, \Sigma), \quad (3.1)$$

where \mathcal{N} denotes a multivariate Gaussian distribution with mean μ and covariance function Σ . In a Bayesian framework, eq (3.1) is interpreted as a posterior distribution, conditioned to the observations $(\mathbf{W}^*, \mathbf{R}^*)$. A Gaussian process is a distribution over functions whose smoothness is defined by the covariance function, computed using a kernel function. Given a set of data $(\mathbf{w}^*, \mathbf{R}^*)$, this allows for building a continuous function to estimate both the reward of a possible candidate and the uncertainties associated with it.

We are interested in evaluating (3.1) on a set of n_E new samples $\mathbf{W} := \{\mathbf{w}_1, \mathbf{w}_2 \dots \mathbf{w}_{n_E}\}$ and let us denote as $\mathbf{R} := \{R_1, R_2 \dots R_{n_E}\}$ the possible outcomes (treated as random variables). Assuming that the possible candidate solutions belong to the same Gaussian process (usually assumed to have zero mean (Rasmussen 2003)) as the observed data $(\mathbf{W}^*, \mathbf{R}^*)$, we have:

$$\begin{pmatrix} \mathbf{R}^* \\ \mathbf{R} \end{pmatrix} \sim \mathcal{N}\left(0, \begin{pmatrix} \mathbf{K}_{**} & \mathbf{K}_* \\ \mathbf{K}_*^T & \mathbf{K} \end{pmatrix}\right), \quad (3.2)$$

where $\mathbf{K}_{**} = \kappa(\mathbf{W}^*, \mathbf{W}^*) \in \mathbb{R}^{n_* \times n_*}$, $\mathbf{K}_* = \kappa(\mathbf{W}, \mathbf{W}^*) \in \mathbb{R}^{n_e \times n_*}$, $\mathbf{K} = \kappa(\mathbf{W}, \mathbf{W}) \in \mathbb{R}^{n_e \times n_e}$ and κ a kernel function.

The prediction in (3.1) can be build using standard rules for conditioning multivariate Gaussian, and the functions μ and Σ in (3.1) becomes a vector μ_* and a matrix Σ_* :

$$\mu_* = \mathbf{K}_*^T \mathbf{K}_R^{-1} \mathbf{R}^* \in \mathbb{R}^{n_E} \quad (3.3)$$

$$\Sigma_* = \mathbf{K} - \mathbf{K}_*^T \mathbf{K}_R^{-1} \mathbf{K}_* \in \mathbb{R}^{n_E \times n_E}, \quad (3.4)$$

where $\mathbf{K}_R = \mathbf{K}_{**} + \sigma_R^2 \mathbf{I}$, with σ_R^2 the expected variance in the sampled data and \mathbf{I} the identity matrix of appropriate size. The main advantage of BO is that the function approximation is sequential, and new predictions improve the approximation of the reward function (i.e. the surrogate model) episode after episode. This makes the GPr- based BO one of the most popular black-box optimization methods for expensive cost functions. Nevertheless, many variants exist and are continuously proposed in the growing field of Hyper-parameter Optimization (HPO) (see [Bergstra et al. \(2013\)](#)). Moreover, in perspective towards possible future hybridization, it is worth noticing that Gaussian processes implemented in classic BO are generic function approximators (like ANNs) and could be used, for example, to attempt approximating the value functions in (2.13) and (2.14). On thus enters the realm of Bayesian Reinforcement learning ([Ghavamzadeh et al. 2015](#)), which, to the authors' knowledge, is fairly unexplored in fluid dynamics.

The second ingredient of BO is a function suggesting where to sample next. Many variants exist ([Frazier 2018](#)), each providing their exploration/exploitation balance. In BO, the exploration seeks to sample in regions of large uncertainty, while exploitation seeks to sample at the best location according to the current function approximation. The most classic function, used in this study, is the expected improvement, defined as ([Rasmussen 2003](#))

$$\text{EI}(\mathbf{x}) = \begin{cases} (\Delta - \xi) \Phi(Z) + \sigma(\mathbf{w}) \phi(Z) & \text{if } \sigma(\mathbf{w}) > 0 \\ 0 & \text{if } \sigma(\mathbf{x}) = 0 \end{cases} \quad (3.5)$$

with $\Delta = \mu(\mathbf{w}) - R(\mathbf{w}^+)$ and $\mathbf{w}^+ = \arg \max_{\mathbf{w}} \hat{R}(\mathbf{w})$ the best sample so far, $\Phi(Z)$ the cumulative distribution (CDF), $\phi(Z)$ the probability density (PDF) of a standard Gaussian and

$$Z = \begin{cases} \frac{\Delta - \xi}{\sigma(\mathbf{w})} & \text{if } \sigma(\mathbf{w}) > 0 \\ 0 & \text{if } \sigma(\mathbf{w}) = 0 \end{cases}. \quad (3.6)$$

Eq (3.5) balances the desire to sample in regions where $\mu(\mathbf{w})$ is closer to $R(\mathbf{w}^+)$ (hence large and positive Δ) versus sampling in regions where $\sigma(\mathbf{w})$ is large. The parameter ξ sets a threshold over the minimal expected improvement that justifies the exploration.

Finally, the method requires the definition of the kernel function and its hyper-parameters, as well as an estimate of σ_y . In this work, the GPr based BO was implemented using the Python API *scikit-optimize* ([Head et al. 2020](#)). The selected kernel function was a Matern kernel with $\nu = 5/2$ (see Chapter 4 from [Rasmussen \(2003\)](#)) which reads:

$$\kappa(\mathbf{x}, \mathbf{x}') = \kappa(r) = 1 + \frac{\sqrt{5}r}{l} + \frac{5r^2}{3l^2} \exp - \frac{\sqrt{5}r}{l}, \quad (3.7)$$

where $r = \|\mathbf{x} - \mathbf{x}'\|_2$ and l the length scale of the process. In general, the performances of the BO strongly depends on the choice of these parameters and their estimation implies knowledge of the cost function, particularly its smoothness or the possible presence of noise. If the computational cost of evaluating an episode is not too large, it is worth running a first exploratory analysis and test the Gaussian process regression on the collected data with various parameters.

Algorithm 22 report the main steps of the Bayesian Optimization through Gaussian Process. Lines (1-9) defines the GPr predictor function, which takes in input the sampled points \mathbf{W}^* , the

associated cumulative rewards \mathbf{R}^* , the testing points \mathbf{W} , and the Kernel function κ in eq. (3.7). This outputs the mean value of the prediction μ_* and its variance Σ_* . The algorithm starts with the initialization of the simulated weights \mathbf{W}^* and rewards \mathbf{R}^* buffers (line 10 and 11). Prior to start the optimization, 10 random weights \mathbf{W}^0 are tested (line 12 and 13). Within the optimization loop, at each iteration, 1000 random points are passed to the GPr predictor, which is also fed with the weight and rewards buffers (line 16 and 17). It provides the associated mean reward value and variance for each weight combination. This information is then passed to an acquisition function (line 17) which outputs a set of values \mathbf{A} associated to the weights \mathbf{W}^+ . The acquisition function is then optimized by an optimizer (line 19). Finally, the best weights are tested in the environment (line 20) and the buffers updated (line 21 and 22).

Algorithm 1 Bayesian Optimization using GPr, adapted from [Rasmussen \(2003\)](#) and [Pedregosa et al. \(2011\)](#)

```

function PREDICTOR( $\mathbf{W}^*$ ,  $\mathbf{R}^*$ ,  $\mathbf{W}$ ,  $\kappa$ )
  Compute  $\mathbf{K} \leftarrow \kappa(\mathbf{W}, \mathbf{W})$ 
  Compute  $\mathbf{K}_{**} \leftarrow \kappa(\mathbf{W}^*, \mathbf{W}^*)$ 
  Compute  $\mathbf{K}_R \leftarrow \mathbf{K}_{**} + \sigma_{w_*} \mathbf{I}$ 
  Compute Cholesky decomposition  $\mathbf{L} \leftarrow \mathbf{K}_R$ 
  Compute  $\alpha \leftarrow \mathbf{L}^T \mathbf{L}^{-1} \mathbf{R}^*$ 
  Compute  $\mathbf{v} \leftarrow \mathbf{L} \mathbf{K}^{-1}$ 
  return mean  $\mu_* \leftarrow \mathbf{K} \alpha$  and variance  $\Sigma_* \leftarrow \mathbf{K} - \mathbf{v}^T \mathbf{v}$ 
end function

Initialize weight buffer  $\mathbf{W}^*$  as null
Initialize function buffer  $\mathbf{R}^*$  as null
Initialize a set of 10 random weights  $\mathbf{W}^0$ 
Collect reward from simulation  $\mathbf{R}^0 \leftarrow \mathbf{R}(\mathbf{W}^0)$ 
Add rewards and weights to buffers  $\mathbf{R}^* \leftarrow \mathbf{R}^0$  and  $\mathbf{W}^* \leftarrow \mathbf{W}^0$ 
for  $k$  in  $(1, N)$  do
  Select 1000 random points  $\mathbf{W}^+$ 
  Evaluate points  $(\mu_*, \Sigma_*) \leftarrow \text{PREDICTOR}(\mathbf{W}^*, \mathbf{R}^*, \mathbf{W}^+, \kappa)$ 
  Compute  $(A, \mathbf{W}^+) \leftarrow \text{ACQFUNCTION}((\mu_*, \Sigma_*))$ 
   $\mathbf{w}^k \leftarrow \underset{\mathbf{w}^+}{\text{argmin}} \text{ACQFUNCTION}(\mathbf{w}^+)$ 
  Collect reward from simulation  $\mathbf{R}^k \leftarrow \mathbf{R}(\mathbf{w}^k)$ 
  Add result to buffers  $\mathbf{R}^* \leftarrow \mathbf{R}^k$  and  $\mathbf{W}^* \leftarrow \mathbf{w}^k$ 
end for

```

3.1.2. Lipschitz global Optimization (LIPO)

Like BO, LIPO relies on a surrogate model to select the next sampling points ([Malherbe & Vayatis 2017](#)). However, LIPO's surrogate function is the much simpler upper bound approximation $U(\mathbf{w})$ of the cost function $R(\mathbf{w})$ ([Ahmed et al. 2020](#)). In the DLIB implementation by [King \(2009\)](#), used in this work, this is given by:

$$U(\mathbf{w}) = \min_{i=1\dots t} \left(R(\mathbf{w}_i) + \sqrt{\sigma_i + (\mathbf{w} - \mathbf{w}_i)^T K (\mathbf{w} - \mathbf{w}_i)} \right), \quad (3.8)$$

where \mathbf{w}_i are the sampled parameters, σ_i are coefficients which account for discontinuities and stochasticity in the objective function, and K is a diagonal matrix that contains the Lipschitz constants k_i for the different dimensions of the input vector. We recall that a function $R(\mathbf{w}) : \mathcal{W} \subseteq$

$\mathbb{R}^{n_w} \rightarrow \mathbb{R}$ is a Lipschitz function if there exists a constant C such that:

$$\|R(\mathbf{w}_1) - R(\mathbf{w}_2)\| \leq C \|\mathbf{w}_1 - \mathbf{w}_2\|, \quad \forall \mathbf{w}_1, \mathbf{w}_2 \in \mathcal{W}, \quad (3.9)$$

where $\|\cdot\|$ is the Euclidean norm on \mathbb{R}^{n_w} . The Lipschitz constant k of $R(\mathbf{w})$ is the smallest C that satisfies the above condition (Davidson & Donsig 2009). In other terms, this is an estimate of the largest possible slope of the function $R(\mathbf{w})$. The values of K and σ_i are found by solving the optimization problem:

$$\begin{aligned} \min_{K, \sigma} \quad & \|K\|_F^2 + 10^6 \sum_{i=1}^t \sigma_i^2 \\ \text{s.t.} \quad & U(\mathbf{w}_i) \geq R(\mathbf{w}_i), \quad \forall i \in [1 \cdots t] \\ & \sigma_i \geq 0, \quad \forall i \in [1 \cdots t] \\ & K_{i,j} \geq 0, \quad \forall i, j \in [1 \cdots d] \\ & \mathbf{K} = \{k_1, k_2, \dots, k_{n_w}\}, \end{aligned} \quad (3.10)$$

where 10^6 is a penalty factor and $\|\cdot\|_F$ is the Frobenius norm.

To compensate for the poor convergence of LIPO in the area around local optima, the algorithm alternates between a global and a local search. If the iteration number is even, it selects the new weights by means of the maximum upper bounding position (MaxLIPO):

$$\mathbf{w}_{k+1} = \arg \max_{\mathbf{w}} (U(\mathbf{w})), \quad (3.11)$$

otherwise, it relies on a Trust Region (TR) method (Powell 2006) based on a quadratic approximation of $R(\mathbf{w})$ around the best weights obtained so far \mathbf{w}^* , i.e:

$$\begin{aligned} \mathbf{w}_{k+1} = \arg \max_{\mathbf{w}} \quad & \overbrace{\left(\mathbf{w}^* + g(\mathbf{w}^*)^T \mathbf{w} + \frac{1}{2} \mathbf{w}^T \mathbf{H}(\mathbf{w}^*) \mathbf{w} \right)}^{m(\mathbf{w}; \mathbf{w}^*)} \\ \text{s.t.} \quad & \|\mathbf{w}_{k+1}\| < d(\mathbf{w}^*) \end{aligned} \quad (3.12)$$

where $g(\mathbf{w}^*)$ is the approximation of the gradient at \mathbf{w}^* ($g(\mathbf{w}^*) \approx \nabla R(\mathbf{w}^*)$), $\mathbf{H}(\mathbf{w}^*)$ is the approximation of the Hessian matrix $(\mathbf{H}(\mathbf{w}^*))_{ij} \approx \frac{\partial^2 R(\mathbf{w}^*)}{\partial w_i \partial w_j}$ and $d(\mathbf{w}^*)$ is the radius of the trust region. If the TR-method converges to a local optimum with an accuracy smaller than ε :

$$|R(\mathbf{w}_k) - R(\mathbf{w}^*)| < \varepsilon, \quad \forall \mathbf{w}_k, \quad (3.13)$$

the optimization goes on with the global search method, until it finds a better optimum.

The algorithm 2 reports the keys steps of the MaxLIPO+TR method. First, a function GLOBALSEARCH function is defined (line 1). This performs a random global search of the parametric space if the random number selected from $S = \{x \in \mathbb{R} \mid 0 \leq x \leq 1\}$ is smaller than p (line3), otherwise it proceeds with MaxLIPO. In our case $p = 0.02$, hence the random search is almost negligible. The upper and lower bound (\mathbf{U}, \mathbf{L}) of the search space are defined in line 10. A buffer object is initialized as empty (line 11). This structure logs the weight \mathbf{w}_i and their relative reward $R(\mathbf{w}_i)$ along the optimization. Within the learning loop (line 17), the second and third weights are selected randomly (line 19). Then, if the iteration number k is even, the algorithm select the next weights via GLOBALSEARCH (line 23), else it relies on the local optimization method (line 31). If the local optimizer reaches an optimum within an accuracy of ε (line 33), the algorithm continues exclusively with GLOBALSEARCH. At the end of each iteration, both the local and the global models are updated with the new weights \mathbf{w}_{k+1} (line 38 and 39).

Algorithm 2 MaxLIPO + TR (Adapted from King (2009))

```

1: function GLOABALSEARCH
2:   if  $x \in_R S > p$  then
3:     Select weights  $\mathbf{w}$  base on MaxLIPO (Eq.(3.11))
4:   else
5:     Select weights  $\mathbf{w}$  randomly
6:   end if
7:   Evaluate reward function  $R(\mathbf{w})$ 
8:   return  $(\mathbf{w}, R(\mathbf{w}))$ 
9: end function
10: Define upper  $\mathbf{U}$  and lower  $\mathbf{L}$  weights' bounds
11: Initialize buffer structure  $\mathbf{W}$  as empty
12: Initialize weights as  $\mathbf{w}_0 = (\mathbf{U} + \mathbf{L})/2$ 
13: Evaluate reward function  $R(\mathbf{w}_0)$ 
14: Initialize the best weight and reward  $(\mathbf{w}^*, R^*) \leftarrow (\mathbf{w}_0, R(\mathbf{w}_0))$ 
15: Add weights and reward to the buffer  $\mathbf{W}(\mathbf{w}_0, R(\mathbf{w}_0))$ 
16: Initialize  $flag \leftarrow \text{False}$ 
17: for  $k$  in  $(1, N_e - 1)$  do
18:   if  $k < 3$  then
19:     Select weights  $\mathbf{w}_k$  randomly
20:     Evaluate reward function  $R(\mathbf{w}_k)$ 
21:   else
22:     if  $flag = \text{True}$  then
23:        $\mathbf{w}_k, R(\mathbf{w}_k) \leftarrow \text{GLOABALSEARCH}()$ 
24:       if  $R(\mathbf{w}_k) > R^*$  then
25:         Set  $flag \leftarrow \text{False}$ 
26:       end if
27:     else
28:       if  $k \bmod 2 = 0$  then
29:          $\mathbf{w}_k, R(\mathbf{w}_k) \leftarrow \text{GLOABALSEARCH}()$ 
30:       else
31:         Select weights  $\mathbf{w}_k$  based on TR (Eq.(3.12))
32:         Evaluate reward function  $R(\mathbf{w}_k)$ 
33:         if  $|R(\mathbf{w}_k) - R^*| < \varepsilon$  (Eq.(3.13)) then
34:           Set  $flag \leftarrow \text{True}$ 
35:           continue
36:         end if
37:       end if
38:       Update upper bound  $U(\mathbf{w})$  with  $\mathbf{w}_k$  (Eq.(3.8))
39:       Update TR  $(m(\mathbf{w}; \mathbf{w}^*))$  Eq.(3.12))
40:     end if
41:   end if
42:   if  $R(\mathbf{w}_k) > R^*$  then
43:     Update  $(\mathbf{w}^*, R^*) \leftarrow (\mathbf{w}_k, R(\mathbf{w}_k))$ 
44:   end if
45:
46: end for
47: EndFor

```

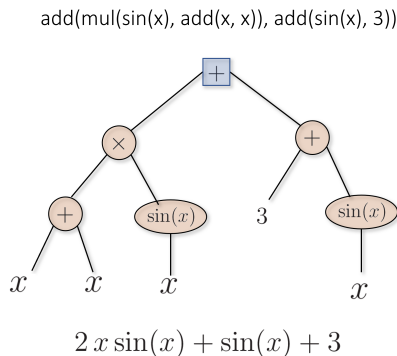


Figure 2: Syntax tree representation of the function $2x \sin(x) + \sin(x) + 3$. This tree has a root '+' and a depth of two. The nodes are denoted with orange circles while the last entries are leaves.

3.2. Genetic Programming

In a Genetic Programming (GP) approach to optimal control, the policy $\mathbf{a} = \pi(\mathbf{s}; \mathbf{w})$ is encoded in the form of a syntax tree. The optimal parameters \mathbf{w}^* are not scalar quantities but lists of numbers and functions which can include arithmetic operations, mathematical functions, Boolean operations, conditional operations or iterative operations. An example of a syntax tree representation of a function is shown in Figure 2. A tree (or *program* in GP terminology) is composed of a root that branches out into nodes (containing functions or operations) throughout various levels. The number of levels defines the *depth* of the tree, and the last nodes are called *terminals* or *leaves*. These contain the input variables or constants. Any combination of branches below the root is called *sub-tree* and can generate a tree if the node becomes a root.

Syntax trees allow encoding complex functions by growing into large structures. The flexible nature of GP allows this architecture to adapt during the training: the user does not provide a parametrization of the policy but a *primitive set*, i.e. the pool of allowed functions, the maximum depth of the tree, and set the parameters of the training algorithm. Then, the GP operates on a population of possible candidate solutions (individuals) and evolves it over various steps (generations) using genetic operations in the search for the optimal tree. Classic operations include elitism, replication, cross-over and mutations, as in Genetic Algorithm Optimization (Haupt & Ellen Haupt 2004).

The implementation of GP in this work was carried out in the **Distributed Evolutionary Algorithms in Python (DEAP)** (Fortin *et al.* 2012) framework. This is an open-source Python library allowing for the implementation of various evolutionary strategies. In this work, we focus on the (μ, λ) algorithm, which we here briefly describe for completeness. The reader is referred to the literature (Banzhaf *et al.* 1997; Vanneschi & Poli 2012; Kober & Peters 2014; Duriez *et al.* 2017) for many other possible implementations of this method.

We used a primitive set of four elementary operations (+, -, /, \times) and four functions (exp, log, sin, cos). The initial population of individuals varied between $n_I = 30$ and $n_I = 50$ candidates depending on the test case and the maximum depth tree was set to 17. In all test cases, the population was initialized using a classic "half-half" approach, whereby half the population is initialized with the *full method* and the rest with the *growth method*. In the full method, the trees are generated with a predefined depth and then filled randomly with nodes and leaves. In the growth method, trees are randomly filled from the roots: because nodes filled with variables or constant are terminals, this approach generates trees of variable depth.

Algorithm 3 shows the relevant steps of the learning process. First, an initial population of random individuals (i.e. candidate control policies) is generated and evaluated (lines 1 and

2) individually. An episode is run for each different tree structure. The population, with their respective rewards (according to eq.2.12), is used to generate a set of λ offspring individuals. The potential parents are selected via *tournament*, where new individuals are generated cross-over (line 9), mutation (line 12) and replication (line 15): each of the new member of the population has a probability p_c , p_m and p_r to arise from any of these three operations, hence $p_c + p_m + p_r = 1$.

The implemented *cross-over strategy* is the simplest (and oldest) *one-point* cross-over. In this technique, two randomly chosen parents are first broken around one randomly selected cross-over point, generating two trees and two subtrees. Then, the offspring is created by replacing the subtree rooted in the first parent with the subtree rooted at the cross-over point of the second parent. Of the two sons, only one is considered in the offspring and the other is discarded. The *mutation strategy* is a *one-point* mutation, in which a random node (sampled with from a uniform distribution) is replaced with any other possible node from the primitive set. The *replication strategy* consists in the direct cloning of one randomly selected parent to the next generation (asexual reproduction). The key difference between the implemented (μ, λ) algorithm over the alternative $(\mu + \lambda)$ is in the tournament selection process: in the first, the tournament only involves the offspring (λ), while in the second also parents could be re-selected.

The new population is created by selecting the best individuals, based on the obtained reward, among the old population $\mathbf{B}^{(i-1)}$ and the offspring $\tilde{\mathbf{B}}$ (line 19).

Algorithm 3 GP $(\mu + \lambda)$ -ES (Adapted from [Beyer & Schwefel \(2002\)](#))

```

1: Initialize population  $\mathbf{B}^{(0)}$  with  $\mu$  random individuals  $\mathbf{a}_i$ .
2: Evaluate fitness  $\mathbf{a}_i \leftarrow (\mathbf{w}_i, R(\mathbf{w}_i))$ 
3: for  $i$  in  $(1, N_e)$  do
4:   Initialize offspring population  $\tilde{\mathbf{B}}$  with  $\lambda$  individuals as empty.
5:   for  $t$  in  $(1, \lambda)$  do
6:     Select random number  $\zeta \in (0, 1)$ 
7:     if  $\zeta < p_c$  then
8:       Random sample two individuals  $(\mathbf{a}_m, \mathbf{a}_n)$  from  $\mathbf{B}^{(i-1)}$ 
9:       Compute offspring individual  $\tilde{\mathbf{a}}_i \leftarrow \mathbf{Mate}(\mathbf{a}_m, \mathbf{a}_n)$ 
10:    else if  $\zeta < (p_c + p_m)$  then
11:      Random sample an individual  $(\mathbf{a}_m)$  from  $\mathbf{B}^{(i-1)}$ 
12:      Compute offspring individual  $\tilde{\mathbf{a}}_i \leftarrow \mathbf{Mutate}(\mathbf{a}_m)$ 
13:    else
14:      Random sample an individual  $(\mathbf{a}_m)$  from  $\mathbf{B}^{(i-1)}$ 
15:      Compute offspring individual  $\tilde{\mathbf{a}}_i \leftarrow \mathbf{a}_m$ 
16:    end if
17:  end for
18:  Evaluate fitness of mated and mutated  $\tilde{\mathbf{a}}_i \leftarrow (\mathbf{w}_i, R(\mathbf{w}_i))$ 
19:  Update population  $\mathbf{B}^{(i)} \leftarrow \mathbf{Select}(\mathbf{B}^{(i)}, \tilde{\mathbf{B}}, \mu)$ 
20: end for

```

3.3. Reinforcement Learning via DDPG

The Deep Deterministic Policy gradient (DDPG) by [Lillicrap et al. \(2015\)](#) is an off-policy actor-critic algorithm using an ANN to learn the policy and an ANN to learn the Q function. In what follows, we call Π - network the first (i.e. the actor) and Q -network the second (i.e. the critic).

The DDP combines the DPG by [Silver et al. \(2014\)](#) and the Deep Q learning (DQN) by [Mnih et al. \(2013, 2015\)](#). The algorithm has evolved into more complex versions such as the Twin Delayed DDPG ([Fujimoto et al. 2018](#)), but in this work we focus on the basic implementation.

The policy encoded in the Π network is deterministic and acts according to the set of weights and biases \mathbf{w}^π , i.e. $\mathbf{a} = \pi(\mathbf{s}_t, \mathbf{w}^\pi)$. The environment is assumed to be stochastic and modelled as a Markov Decision Process. Therefore, (2.14) must be modified to introduce an expectation operator:

$$Q^\pi(\mathbf{s}_t, \mathbf{a}_t) = \mathbb{E}_{\mathbf{s}_t, \mathbf{s}_{t+1} \sim E} [r(\mathbf{s}_t, \mathbf{a}_t) + \gamma Q^\pi(\mathbf{s}_{t+1}, \mathbf{a}_{t+1}^\pi)], \quad (3.14)$$

where the policy is intertwined in the action state relation, i.e. $Q^\pi(\mathbf{s}_{t+1}, \mathbf{a}_{t+1}) = Q^\pi(\mathbf{s}_{t+1}, \mathbf{a}^\pi(\mathbf{s}_{t+1}))$ and having used the shorthand notation $\mathbf{a}_{t+1}^\pi = \pi(\mathbf{s}_{t+1}, \mathbf{w}^\pi)$. Because the expectation operator in (3.14) solely depends on the environment (E in the expectation operator), it is possible to decouple the problem of learning the policy π from the problem of learning the function $Q^\pi(\mathbf{s}_t, \mathbf{a}_t)$. Concretely, let $Q(\mathbf{s}_t, \mathbf{a}_t; \mathbf{w}^Q)$ denote the prediction of Q function by the Q network, defined with weights and biases \mathbf{w}^Q and let \mathcal{T} denote a set of N transitions $(\mathbf{s}_t, \mathbf{a}_t, \mathbf{s}_{t+1}, r_{t+1})$ collected through (any) policy. The performances of the Q-network can be measured as

$$J^Q(\mathbf{w}^Q) = \mathbb{E}_{\mathbf{s}_t, \mathbf{a}_t, r_t \sim \mathcal{T}} \left[\left(Q(\mathbf{s}_t, \mathbf{a}_t; \mathbf{w}^Q) - y_t \right)^2 \right], \quad (3.15)$$

where

$$y_t = r(\mathbf{s}_t, \mathbf{a}_t) + \gamma Q(\mathbf{s}_{t+1}, \mathbf{a}_{t+1}; \mathbf{w}^Q). \quad (3.16)$$

Equation (3.15) measures how closely the prediction of the Q network satisfies the discrete Bellman equation (2.14). The training of the Q network can be carried out using standard stochastic gradient descent methods using the back-propagation algorithm (Kelley 1960) to evaluate the gradient $\partial_{\mathbf{w}^Q} J^Q$.

The training of the Q-network gives the off-policy flavour to the DDPG because it is carried out with an exploratory policy that might largely differ from the policy that will be finally selected. Nevertheless, because the training of the Q-network is notoriously unstable, Mnih *et al.* (2013, 2015) introduced the use of a *replay buffer* to leverage accumulated experience (previous transitions) and a *target network* to under-relax the update of the weights during the training. Both the computation of the cost function in (3.15) and its gradient are performed over a random batch of transitions \mathcal{T} in the replay buffer \mathcal{R} .

The DDPG combines the Q-network prediction with a policy gradient approach to train the Π -network. This is inherited from the DPG by Silver *et al.* (2014), who have shown that, given

$$J^\pi(\mathbf{w}^\pi) = \mathbb{E}_{\mathbf{s}_t \sim E, \mathbf{a}_t \sim \pi} [r(\mathbf{s}_t, \mathbf{a}_t)] \quad (3.17)$$

the expected return from the initial condition, the gradient with respect to the weights in the Π network is:

$$\partial_{\mathbf{w}^\pi} J^\pi = \mathbb{E}_{\mathbf{s}_t \sim E, \mathbf{a}_t \sim \pi} [\partial_{\mathbf{a}} Q(\mathbf{s}_t, \mathbf{a}_t; \mathbf{w}^Q) \partial_{\mathbf{w}^\pi} \mathbf{a}(\mathbf{s}_t; \mathbf{w}^\pi)]. \quad (3.18)$$

Both $\partial_{\mathbf{a}} Q(\mathbf{s}_t, \mathbf{a}_t; \mathbf{w}^Q)$ and $\partial_{\mathbf{w}^\pi} \mathbf{a}(\mathbf{s}_t; \mathbf{w}^\pi)$ can be evaluated via back-propagation, on the Q network and the Π network respectively. The main extension of DDPG over DPG is the use of DQN for the estimation of the Q function.

In this work, we implement the DDPG using KERAS API in PYTHON with three minor modifications to the original algorithm. The first is a clear separation between the exploration and the exploitation phases. In particular, we introduce a number of exploratory episodes $n_{Ex} < n_{Ep}$ and the action is computed as

$$\mathbf{a}(\mathbf{s}_t) = \mathbf{a}(\mathbf{s}_t; \mathbf{w}^\pi) + \eta(\text{ep}) \mathcal{E}(t; \theta, \sigma^2), \quad (3.19)$$

where $\mathcal{E}(t; \theta, \sigma)$ is an exploratory random process characterized by a mean θ and variance σ^2 .

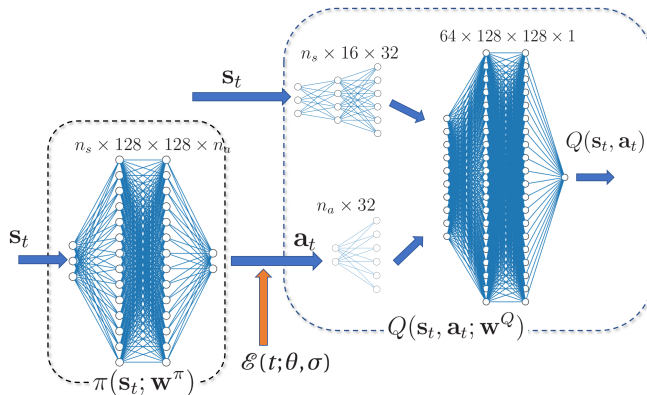


Figure 3: ANN Architecture of the DDPG implementation analyzed in this work. The illustrated architecture is the one used for the test case in section 4.3. During the exploration phase, the two networks are essentially decoupled by the presence of the stochastic term \mathcal{E} that leads to exploration of the action space.

This could be the time-correlated (Uhlenbeck & Ornstein 1930) noise or white noise, depending on the test case at hand (see Sec. 4). The transition from exploration to exploitation is governed by the parameter η ep, which is taken as $\eta(\text{ep}) = 1$ if $\text{ep} < n_{Ex}$ where $d^{\text{ep} - n_{Ex}}$ if $\text{ep} > n_{Ex}$. This decaying term for $\text{ep} > n_{Ep}$ progressively reduces the exploration and the coefficient d controls how rapidly this is done.

The second modification is in the selection of the transitions from the replay buffer \mathcal{R} that are used to compute the gradient $\partial_{\mathbf{w}^Q} J^Q$. While the original implementation selects these randomly, we implement a simple version of the prioritized experience replay from Schaul *et al.* (2018). The idea is to prioritize, while sampling from the replay buffer, those transitions which have lead to the largest improvement in the network performances. These can be measured in terms of Temporal Difference Error (or TD-Error):

$$\delta = r_t + \gamma Q(\mathbf{s}_{t+1}, \mathbf{a}_{t+1}^\pi; \mathbf{w}^Q) - Q(\mathbf{s}_t, \mathbf{a}_t; \mathbf{w}^Q). \quad (3.20)$$

Intuitively, this quantity measures how much a transition was *unexpected*. As discussed by Schaul *et al.* (2018), it can be shown that this increases the learning rate of the algorithm towards the steepest gradients $\partial_{\mathbf{w}^Q} J^Q$, and helps overcoming local minima. Ranking the transitions in decreasing order of TD error δ , the sampling is performed following a triangular distribution which assigns the highest probability $p(n)$ to the transition with the largest TD error δ .

The third modification, extensively discussed in previous works on reinforcement learning for flow control (Rabault & Kuhnle 2019; Tang *et al.* 2020; Rabault *et al.* 2020), is the implementation of a moving average of the actions. In other words, an action is performed for K consecutive interactions with the environment, which in our work occur at every simulation's time step.

We illustrate the neural network architecture employed in this work in Figure 3. The scheme in Figure shows how the Π network and the Q network are interconnected: intermediate layers map the current state and the action (output by the Π network) to the core of the Q network. For plotting purposes, the number of neurons in the figure is much smaller than the one actually used and indicated in the figure. The Π network has two hidden layers with 128 neurons each, while the input and output depends on the test cases considered (see Sec. 4). Similarly, the Q network has two hidden layers with 128 neurons each and intermediate layers as shown in the figure. During the exploration phase, the presence of the stochastic term in the action selection decouples the two networks.

We recall the main steps of the DDPG algorithm in algorithm 4. After random initialization of the weights in both network and the initialization of the replay buffer (lines 1-3), the loop over episodes and time steps proceeds as follows. The agent begins from an initial state (line 5), which is simply the final state of the system from the previous episode or the last state from the uncontrolled dynamics. In other words, none of the investigated environments has a terminal state and no re-initialization is performed.

Within each episode, at each time step, the DDPG takes actions (lines 7-12) following (3.19) (line 8) or copying the previous action (line 10). After storing the transition in the replay buffer (lines 13), these are ranked based on the associated TD error δ (line 14). This is used to sample a batch of N transitions following a triangular distribution favouring the transitions with the highest δ . The transitions are used to compute the cost functions $J^Q(\mathbf{w}^Q)$ and $J^\pi(\mathbf{w}^\pi)$ and their gradients $\partial_{\mathbf{w}^Q} J(\mathbf{w}^Q)$, $\partial_{\mathbf{w}^\pi} J(\mathbf{w}^\pi)$ and thus update the weights following a gradient ascent (lines 17 and 19). This operation is performed on the 'current networks' (defined by the weights \mathbf{w}^π and \mathbf{w}^Q). However, the computation of the critic losses J^Q is performed with the prediction y_t from the target networks (defined by the weights $\mathbf{w}^{\pi'}$ and $\mathbf{w}^{Q'}$). The targets are under-relaxed updates of the network weights computed at the end of each episode (lines 21-22).

The reader should notice that, differently from the other optimization-based approaches, the update of the policy is performed *at each time step* and not at the end of the episode.

Algorithm 4 DDPG (Adapted from Lillicrap *et al.* (2015))

```

Initialize  $Q(\mathbf{s}, \mathbf{a}; \mathbf{w}^Q)$  and  $\pi(\mathbf{s}; \mathbf{w}^\pi)$  with random  $\mathbf{w}^Q$  and  $\mathbf{w}^\pi$ .
2: Initialize targets  $\mathbf{w}^{Q'} \leftarrow \mathbf{w}^Q$  and  $\mathbf{w}^{\pi'} \leftarrow \mathbf{w}^\pi$ .
   Initialize replay Buffer  $\mathcal{R}$  as empty.
4: for ep in  $(1, n_E)$  do
   Observe initial state  $\mathbf{s}_0$ 
6:   for  $t$  in  $(1, T)$  do
     if  $t = 1$  or  $\text{mod}(t, K) = 0$  then
8:        $\mathbf{a}_t = \mathbf{a}(\mathbf{s}_t; \mathbf{w}^\pi) + \eta(\text{ep}) \mathcal{N}(t; \theta, \sigma)$ 
     else
10:         $\mathbf{a}_t = \mathbf{a}_{t-1}$ 
     end if
12:   Execute  $\mathbf{a}_t$ , get  $r_t$  and observe  $\mathbf{s}_{t+1}$ 
   Store the transitions  $(\mathbf{s}_t, \mathbf{a}_t, r_t, \mathbf{s}_{t+1})$  in  $R$ 
14:   Rank the transition by TD error  $\delta$ 
   Select  $N$  transitions in  $R$ , favouring the highest  $\delta$ 
16:   Compute  $y_t = r_t + \gamma Q'(\mathbf{s}_t, \pi(\mathbf{s}_t, \mathbf{w}^{\pi'}))$ 
   Compute  $J^Q = \mathbb{E}(y_t - Q(\mathbf{s}_t, \pi(\mathbf{s}_t, \mathbf{w}^\pi)))$  and  $\partial_{\mathbf{w}^Q} J^Q$ 
18:   Update  $\mathbf{w}^Q \leftarrow \mathbf{w}^Q + \alpha_q \partial_{\mathbf{w}^Q} J^Q$ 
   Compute  $J^\pi(\mathbf{w}^{\pi'})$  and  $\partial_{\mathbf{w}^{\pi'}} J^\pi$ 
20:   Update  $\mathbf{w}^\pi \leftarrow \mathbf{w}^\pi + \alpha_q \partial_{\mathbf{w}^{\pi'}} J^\pi$ 
   Update targets in Q:  $\mathbf{w}^{Q'} \leftarrow \tau \mathbf{w}^{Q'} + (1 - \tau) \mathbf{w}^Q$ 
22:   Update targets in  $\pi$ :  $\mathbf{w}^{\pi'} \leftarrow \tau \mathbf{w}^{\pi'} + (1 - \tau) \mathbf{w}^\pi$ 
   end for
24: end for

```

In our implementation, we used the Adam optimizer for training the ANN's with a learning rate of 10^{-3} and $2 \cdot 10^{-3}$ for the actor and the critic, respectively. The discount factor was set to $\gamma = 0.99$ and the soft-target update parameters is $\tau = 5 \cdot 10^{-3}$. For what concerns the neural networks architecture, the hidden layers used the rectified non-linear activation function, while

the actor output was bounded relying on a hyperbolic tangent (tanh). The actor's network was $n_s \times 256 \times 256 \times n_a$, where n_s is the number of states and n_a is the number of actions expected by the environment. Finally, the critic's network concatenates two networks. The first, from the action taken by the agent composed as $n_a \times 64$. The states are elaborated in two layers: $n_s \times 32 \times 64$. These are concatenated and expanded by means of two layers $256 \times 256 \times 1$ - where the output is the value estimated.

4. Test Cases

4.1. A OD Frequency Cross-Talk Problem

The first selected test case is a system of nonlinear ODEs reproducing one of the main features of turbulent flows: the frequency cross-talk. This control problem was proposed and extensively analysed by [Duriez et al. \(2017\)](#). It essentially consists in stabilizing two coupled oscillators which describe the time evolution of four leading Proper Orthogonal Decomposition (POD) modes of the flow past a cylinder. The model is known as generalized mean field model ([Dirk et al. 2009](#)) and it was used to describe the stabilizing effect of low frequency forcing on the wave flow past a bluff body ([Aleksic et al. 2010](#); [Pastoor et al. 2008](#)).

The set of ODEs which describes the evolution of the four POD modes ($\mathbf{s}(t) = [s_1(t), s_2(t), s_3(t), s_4(t)]^T$), where (s_1, s_2) and (s_3, s_4) are the first and second oscillator, reads:

$$\dot{\mathbf{s}} = \mathbf{F}(\mathbf{s})\mathbf{s} + \mathbf{a}, \quad (4.1)$$

where \mathbf{a} is the forcing vector with a single scalar component interacting with the second oscillator (i.e., $\mathbf{a} = [0, 0, 0, a]^T$) and the matrix $\mathbf{F}(\mathbf{s})$ is given by:

$$\mathbf{F}(\mathbf{s}) = \begin{bmatrix} \sigma(\mathbf{s}) & -1 & 0 & 0 \\ 1 & \sigma(\mathbf{s}) & 0 & 0 \\ 0 & 0 & -0.1 & -10 \\ 0 & 0 & 10 & -0.1 \end{bmatrix}, \quad (4.2)$$

and σ models the coupling between the two oscillators:

$$\sigma(\mathbf{s}) = 0.1 - E_1 - E_2, \quad (4.3)$$

where E_1 and E_2 are the energy of the first and the second oscillator given by:

$$E_1 = s_1^2 + s_2^2 \quad E_2 = s_3^2 + s_4^2. \quad (4.4)$$

This nonlinear link is the essence of the frequency cross-talk and challenges linear control methods based on linearization of the dynamical system.

The initial conditions are set to $\mathbf{a}(0) = [0.01, 0, 0, 0]^T$. Without actuation, the system reaches a 'slow' limit cycle involving the first oscillator (a_1, a_2) while the second vanishing ($(a_3, a_4) \rightarrow 0$). The evolution of the oscillator (a_1, a_2) with no actuation is shown in [Figure 4a](#). [Figure 4b](#) shows the time evolution of σ , which $\sigma \rightarrow 0$ as the system naturally reaches the limit cycle.

The governing equations (Eq.4.1) were solved using scipy's package odeint with a time step of $\Delta t = \pi/50$. This time step is smaller than the one by [Duriez et al. \(2017\)](#) ($\Delta t = \pi/10$), as we observed this had an impact on the training performances (aliasing in LIPO and BO optimization). Finally, the actions are clipped to the range $a_k \in [-1, 1]$.

The actuators' goal is to bring to rest the first oscillator, leveraging on the non-linear connection between the two oscillators while using the least possible actuation. In this respect, the optimal control law, similarly to [Duriez et al. \(2017\)](#), is the one that minimizes the cost function:

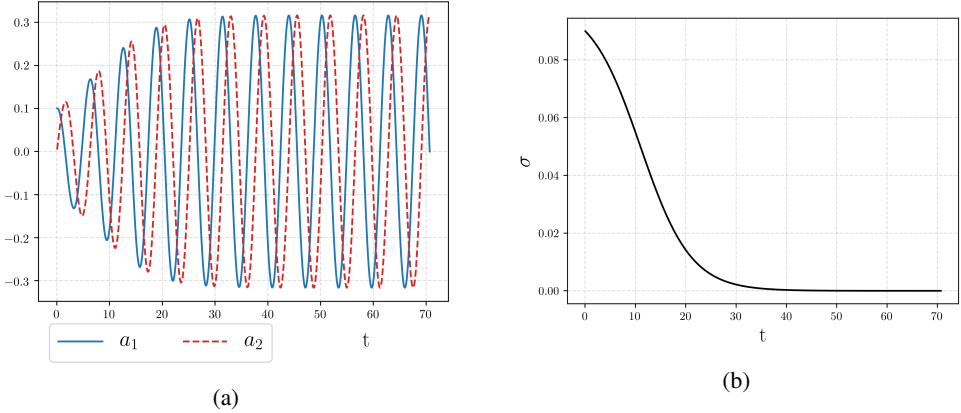


Figure 4: Evolution of the oscillator (a_1, a_2) (a) of the variable σ (4.3) (b) in the OD test case in absence of actuation ($b = 0$). As $\sigma \approx 0$, the system naturally evolves towards a ‘slow’ limit cycle.

$$J = J_a + \gamma J_b = \overline{s_1^2 + s_2^2} + \alpha \overline{a^2}$$

$$\text{where } \overline{f(t)} = \frac{1}{40\pi} \int_{20\pi}^{60\pi} f(t') dt', \quad (4.5)$$

where α is a coefficient set to penalize large actuations and is set to 10^{-2} .

The time interval of an episode is here set to $t \in [20\pi, 60\pi]$, thus much shorter than the one used by Duriez *et al.* (2017). This duration was considered sufficient, as it allows the system to reach the limit cycle and to observe approximately 20 periods of the slow oscillator. To reproduce the same cost function in a reinforcement learning framework, we rewrite (4.5) as a cumulative reward, replacing the integral mean with the arithmetic average and setting:

$$J = \frac{1}{n_t} \sum_{k=0}^{n_t-1} s_{1k}^2 + s_{2k}^2 + \alpha a_k^2 = - \sum_{k=0}^{n_t-1} r_t = -R, \quad (4.6)$$

with r_t the environment’s reward at each time step.

For the BO and LIPO optimizers, the control law is defined as a quadratic form of the four system’s states:

$$\pi(\mathbf{s}; \mathbf{w}) := \mathbf{g}_w^T \mathbf{s} + \mathbf{s}^T \mathbf{H}_w \mathbf{s}, \quad (4.7)$$

with $\mathbf{g}_w \in \mathbb{R}^4$ and $\mathbf{H}_w \in \mathbb{R}^{4 \times 4}$. The weight vectors associated to this policy is thus $\mathbf{w} \in \mathbb{R}^{20}$ and it collects all the entries in \mathbf{g}_w and \mathbf{H}_w . For later reference, the labelling of the weights is as follows:

$$\mathbf{g}_k = \begin{bmatrix} w_1 \\ w_2 \\ w_3 \\ w_4 \end{bmatrix} \quad \text{and} \quad \mathbf{H}_k = \begin{bmatrix} w_5 & w_9 & w_{13} & w_{17} \\ w_6 & w_{10} & w_{14} & w_{18} \\ w_7 & w_{11} & w_{15} & w_{19} \\ w_8 & w_{12} & w_{16} & w_{20} \end{bmatrix}. \quad (4.8)$$

Both LIPO and BO seek for the optimal weights in the range $[-3, 3]$. BO was set up with a Matern kernel (see (3.7)) with a smoothness parameter $\nu = 1.5$, a length scale of 0.01, an acquisition function based on the expected improvement and an exploitation-exploration (see (3.5)) trade-off parameter ξ of 0.1. All the simulations were run for 100 episodes except for the

GP, which was set with an initial population of 30 individuals ($\mu = 30$), an offspring size of 60 ($\lambda = 60$) and it was trained for 20 generations.

In the DDPG implementation, we scale the reward stored in the replay buffer (r_t^{RB}) with the environment reward values obtained until then, which are stored in a dynamical vector $r_{log} = [r_1, r_2, \dots, r_t]$:

$$r_t^{RB} = \frac{r_t - \bar{r}_{log}}{std(r_{log}) + 1e - 10} \quad (4.9)$$

where \bar{r}_{log} is the mean value and $std(r_{log})$ is the standard deviation. The stored reward are then ordered based on their temporal difference (see (3.20)), promoting experiences with high error. The experiences are collected with an exploration strategy structured into three parts: a heavy explorative phase (until episode 30) during which the noise is clipped in the range $[-0.8, 0.8]$ with $\eta = 1$ (see (3.19)). An off-policy exploration phase (between episode 30 and 55) with a noise signal clipped in the range $[-0.25, 0.25]$ with a magnitude of 0.25 and a pure exploitation phase where the noise is almost negligible. As explorative signal, we used a white noise with a standard deviation of 0.5.

4.2. Control of the viscous Burgers's equation

We consider Burger's equation because it offers a simple 1D problem combining nonlinear advection and diffusion. The problem set is:

$$\begin{aligned} \partial_t u + u \partial_x u &= \nu \partial_{xx} u + f(x, t) + c(x, t), \\ u(x, 0) &= u_0 \\ \partial_x u(0, t) &= \partial_x u(L, t) = 0 \end{aligned} \quad (4.10)$$

where $(x, t) \in (0, L) \times (0, T]$ with $L = 20$ and $T = 15$ is the episode length, $\nu = 0.9$ is the kinematic viscosity, $f(x, t)$ is a disturbance term and $c(x, t)$ is the control function. These are both Gaussian functions in space, modulated by a time varying amplitude:

$$f(x, t) = A \sin(2\pi f_p t) \cdot \mathcal{N}(x - x_f, \sigma), \quad (4.11)$$

$$c(x, t) = a(t) \cdot \mathcal{N}(x - x_a, \sigma), \quad (4.12)$$

taking $A = 100$ and $f_p = 0.5$ for the disturbance's amplitude and frequencies and denoting as $a(t)$ the action function provided by the controller. The disturbance and the controller action are centered at $x_f = 6.6$ and $x_c = 13.2$ respectively and have $\sigma = 0.2$. The uncontrolled system produces a set of nonlinear waves propagating in both directions at approximately constant velocities. The objective of the controller is to neutralize the waves downstream the control location, i.e. for $x > x_c$. The controller is informed by three observations, located at $x = 8, 9, 10$. The action is then computed as

$$a(t) = w_0 u(8, t) + w_1 u(9, t) + w_2 u(10, t). \quad (4.13)$$

The controller's performance is measured by the reward function:

$$r(t) = -\left(\ell_2(u_t)_{\Omega_r} + \alpha \cdot a(t)^2\right) \quad (4.14)$$

where $\ell_2(\cdot)_{\Omega_r}$ is the Euclidean norm of the displacement u_t at time step t over a portion of the domain $\Omega_r = \{x \in \mathbb{R} | 15.4 \leq x \leq 16.4\}$ called reward area, α is a penalty coefficient and a_t is the value of the control action selected by the controller. The cumulative reward is computed with a discount factor $\gamma = 1$ while the penalty in the actions was set to $\alpha = 100$. Figure 5 shows the evolution of the uncontrolled system in a contour plot in the space-time domain, recalling the location of perturbation, action, observation and reward area.

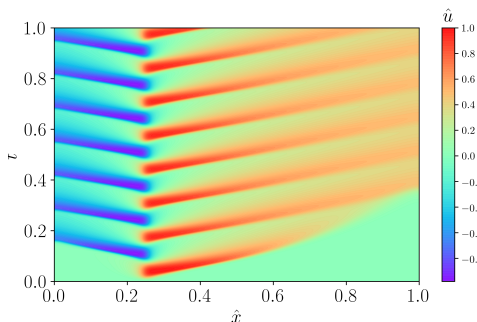


Figure 5: Contour plot of the spatio-temporal evolution of u in (4.10) for the uncontrolled problem, i.e $c(x, t) = 0$. The perturbation is centered at $x = 6.6$ (red continuous line) while the control law is centered at $x = 13.2$. The dashed black lines visualize the location of the observation points while the region within the white dash-dotted line is used to evaluate the controller performance.

Eq.(4.10) was solved using Crank–Nicolson’s method. The Neumann boundary conditions are enforced using ghost cells, and the system is solved at each time step via the banded matrix solver `solve_banded` from the python library `scipy`. The mesh consists of $n_x = 1000$ points and the time stepping is $\Delta t = 0.01$, thus leading to $n_t = 1500$ steps per episode.

Both LIPO and BO optimizers operate within the bounds $[-0.1, 0.1]$ for the weights to avoid saturation in the control action. The overall set-up of the BO is the same as the one used in the 0D test case. For the GP, the selected evolutionary strategy is $(\mu + \lambda)$, with the initial population of 10 individuals $\mu = 10$ and an offspring $\lambda = 20$. The DDPG agent set-up relies on the same reward normalization and buffer prioritization presented for the previous test case. However, the trade-off between exploration and exploitation was handled differently: the random noise term in (3.19) is set to zero every $N = 3$ episodes to prioritize exploitation. This noise term was taken as an Ornstein-Uhlenbeck, time-correlated noise with $\theta = 0.15$ and $dt = 1e - 3$ and its contribution was clipped in $[-0.3, 0.3]$.

4.3. Control of the von Kármán street behind a 2D cylinder

The third test case is controlling the 2D viscous and incompressible flow past a cylinder in a channel. The flow past a cylinder is a classic benchmark for bluff body wakes (Zhang *et al.* 1995; Noack *et al.* 2003), exhibiting a supercritical Hopf bifurcation leading to the well known von Kármán vortex street. The cylinder wake configuration within a narrow channel has been extensively used for CFD benchmark purposes (Schäfer *et al.* 1996) and as a test case for flow control techniques (Rabault *et al.* 2019; Tang *et al.* 2020; Li & Zhang 2021).

We consider the same control problem as in Tang *et al.* (2020), sketched in Figure 6. The computational domain is a rectangle of width L and height H , with a cylinder of diameter $D = 0.01\text{m}$ located slightly off the symmetric plane of the channel (cf. Fig. 6). This asymmetry triggers the development of vortex shedding.

The reference system is located at the center of the cylinder. At the inlet ($x = -2D$), a parabolic velocity profile is imposed:

$$u_{inlet} = \frac{-4U_m}{H^2} (y^2 - 0.1Dy - 4.2D^2), \quad (4.15)$$

where $U_m = 1,5\text{m/s}$. This leads to a Reynolds number of $Re = \bar{U}D/\nu = 400$ using the mean inlet velocity $\bar{U} = 2/3U_m$ as a reference and taking a kinematic viscosity of $\nu = 2.5e - 4\text{m}^2/\text{s}$. It is worth noticing that this is much higher than $Re = 100$ considered by Jin *et al.* (2020), who defines the Reynolds number based on the maximum velocity.

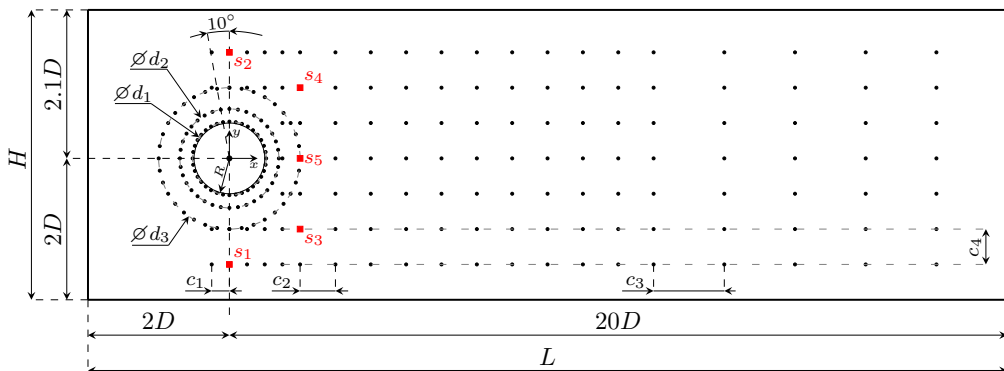


Figure 6: Geometry and observations probes for the 2D von Kármán street control test case. The 256 observations used by [Tang et al. \(2020\)](#) are shown with black markers. These are organized in three concentric circles (diameters $1 + 0.002/D$, $1 + 0.02D$ and $1 + 0.05D$) around the cylinder and three grids (horizontal spacing $c_1 = 0.025/D$, $c_2 = 0.05/D$ and $c_3 = 0.1/D$). All the grids have the same vertical distance between adjacent points ($c_4 = 0.05/D$). The five observations used in this work (red markers) have coordinates $s_1(0, -1.5)$, $s_2(0, 1.5)$, $s_3(1, -1)$ and $s_4(1, 1)$ and $s_5(1, 0)$. Each probe samples the pressure field.

The computational domain is discretized with an unstructured mesh refined around the cylinder, and the incompressible Navier-Stokes equations are solved using the incremental pressure correction scheme (IPCS) method in the FEniCS platform ([Alnæs et al. 2015](#)). The mesh consists of 25865 elements and simulation time step is set to $\Delta t = 1e - 4[s]$ to respect the CFL condition. The reader is referred to [Tang et al. \(2020\)](#) for more details on the numerical set-up and the mesh convergence analysis.

In the control problem, every episode is initialized from a snapshot that has reached a developed shedding condition. This was computed by running the simulation without control for $T = 0.91s = 3T^*$, where $T^* = 0.303s$ is the vortex shedding period. We computed T^* by analysing the period between consecutive pressure peaks observed by probe s_5 of an uncontrolled simulation. The result is the same as the one found by [Tang et al. \(2020\)](#), who performed a Discrete Fourier Transform (DFT) of the drag coefficient.

The instantaneous drag and lift on the cylinder are calculated via the surface integrals:

$$F_D = \int (\sigma \cdot n) \cdot e_x dS, \quad F_L = \int (\sigma \cdot n) \cdot e_y dS, \quad (4.16)$$

where S is the cylinder surface, σ is the Cauchy stress tensor, n is the unit vector normal to the cylinder surface, e_x and e_y are the unit vectors of the x and y axes respectively. The drag and lift coefficient are calculated as $C_D = 2F_D/(\rho \bar{U}^2 D)$ and $C_L = 2F_L/(\rho \bar{U}^2 D)$ respectively.

The control action consists in injecting/removing fluid from four synthetic jets positioned on the cylinder boundary as shown in Figure 7. The jets are symmetric with respect to the horizontal and vertical axes. These are located at $\theta = 75^\circ, 105^\circ, 255^\circ, 285^\circ$ and have the same width $\Delta\theta = 15^\circ$. The velocity profile in each of the jets is taken as:

$$u_{jet}(\theta) = \frac{\pi}{\Delta\theta D} Q_i^* \cos\left(\frac{\pi}{\Delta\theta}(\theta - \theta_i)\right) \quad (4.17)$$

where θ_i is the radial position of the i-th jet and Q_i^* is the imposed flow rate. Eq (4.17) respects the non-slip boundary conditions at the walls. To ensure a zero-net mass injection at every time step, the flow rates are mean shifted as $Q_i^* = Q_i - \bar{Q}$ with $\bar{Q} = \frac{1}{4} \sum_i Q_i$ the mean value of the four flow rates.

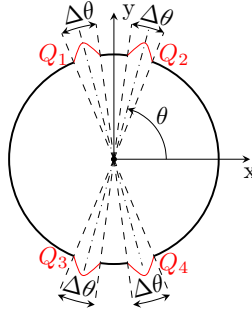


Figure 7: Location of the four control jets for the 2D von Kármán street control test case. These are located at $\theta = 75^\circ, 105^\circ, 255^\circ, 285^\circ$ and have width $\Delta\theta = 15^\circ$. The velocity profile is defined as in (4.17), with flow rate defined by the controller and shifted to have zero-net mass flow.

The flow rates in the four nozzle constitute the action vector, i.e. $\mathbf{a} = [Q_1, Q_2, Q_3, Q_4]^T$ in the formalism of Section 2. To avoid abrupt changes in the boundary conditions, the control action is kept constant for a period of $T_c = 10\Delta t = 1e - 3[s]$. This is thus equivalent to having a moving average filtering of the controller actions with impulse response of length $N = 10$. The frequency modulation of such a filter is

$$H(\omega) = \frac{1}{10} \left| \frac{\sin(5\omega)}{\sin(\omega/2)} \right| \quad (4.18)$$

with $\omega = 2\pi f/f_s$. The first zero of the filter is located at $\omega = 2\pi/5$, thus $f = f_s/5 = 2000Hz$, while the attenuation at the shedding frequency is negligible. Therefore, this filtering allows the controller to act freely within the range of frequencies of interest to the control problem, while preventing abrupt changes that might compromise the stability of the numerical solver. Each episode has a duration of $T = 0.91s$, corresponding to 2.73 periods of the vortex shedding in uncontrolled conditions. This allows having 91 interactions per episode (i.e. 33 interactions per vortex shedding period).

The actions are linked to the pressure measurements (observations of the flow) in various locations. In the original environment by Tang *et al.* (2020), 256 probes were used, similarly to Rabault *et al.* (2019). The locations of these probes are shown in Figure 6 using black markers. In this work, we reduce the set of probes to $n_s = 5$. A similar configuration was analyzed by Rabault *et al.* (2019) although using different locations. In particular, we kept the probes s_1 and s_2 at the same x coordinate, but we moved them further away from the cylinder wall to reduce the impact of the injection on the sensing area. Moreover, we slightly move the sensors s_3, s_4, s_5 downstream in regions where the vortex shedding is more strongly present.

The locations used in this work are recalled in Figure 6. The state vector, in the formalism of Section 2, is thus the set of pressure at the probe locations, $\mathbf{s} = [p_1, p_2, p_3, p_4, p_5]^T$. For the optimal control strategy identified via the BO and LIPO algorithms in Section 3.1.1 and 3.1.2, a linear control law is assumed, hence $\mathbf{a} = \mathbf{W}\mathbf{s}$, with the 20 weight coefficients labelled as follows

$$\begin{bmatrix} Q_1 \\ Q_2 \\ Q_3 \\ Q_4 \end{bmatrix} = \begin{bmatrix} w_1 & w_2 & w_3 & w_4 & w_5 \\ w_6 & w_7 & w_8 & w_9 & w_{10} \\ w_{11} & w_{12} & w_{13} & w_{14} & w_{15} \\ w_{16} & w_{17} & w_{18} & w_{19} & w_{20} \end{bmatrix} \begin{bmatrix} p_1 \\ p_2 \\ p_3 \\ p_4 \\ p_5 \end{bmatrix}. \quad (4.19)$$

It is worth noticing the zero-net mass condition enforced by removing the average flow rate

from each action could be easily imposed by constraining all columns of \mathbf{W} to add up to zero. For example, setting the symmetry $w_1 = -w_{11}$, $w_6 = -w_{16}$, etc. (leading to $Q_1 = -Q_3$ and $Q_2 = -Q_4$) allows for halving the dimensionality of the problem, thus significantly improving the optimization performances. Nevertheless, one has infinite ways of embedding the zero-net mass condition. We do not impose any and let the control problem act in \mathbb{R}^{20} .

Finally, the instantaneous reward r_t is defined as

$$r_t = \langle F_D \rangle_T - \alpha |\langle F_L \rangle_T| \quad (4.20)$$

where $\langle \bullet \rangle_{T_c}$ is the moving average over $T_c = 10\Delta t$ and α is the usual penalization parameter set to $\alpha = 0.2$. This penalization term prevents the control strategies from relying on the high lift flow configurations [Rabault et al. \(2019\)](#). The cumulative reward was given with $\gamma = 1$.

The search space for the optimal weights in LIPO and BO was bounded to $[-1, 1]$. Moreover, the action resulting from the linear combination of such weights with the states collected in the i -th interaction was scaled with a factor $\chi = 2e - 3$, to avoid numerical instabilities. The BO settings are the same as in the previous test-cases, exception made for the smoothness parameter ν that was reduced to $\nu = 1.5$. On the GP side, the evolutionary strategy applied was the *eaSimple*'s ([Back & Michalewicz 2000](#)) implementation in Deap - with hard-coded elitism to preserve the best individuals. It is noted how one population per each jet was used, to retain generality in the description performed by GP and not to misrepresent its proposed solution.

Finally, the DDPG agent was trained using the same exploration policy of the Burgers' test-case, alternating 20 exploratory episodes with the $\eta = 1$ and 45 exploitative episodes with $\eta = 0$ (c.f eq (3.19)). During the exploratory phase, an episode with $\eta = 0$ is taken every $N = 4$ episodes and the policy weights are saved. We used the Ornstein-Uhlenbeck time correlated noise with $\theta = 0.1$ and $dt = 1e - 2$ in eq. (3.19), clipped in $[-0.5, 0.5]$.

5. Results and Discussions

We present here the outcomes of the different control algorithms in terms of learning curves and control actions for the three investigate test cases. Given the heuristic nature of these control strategies, we ran several training sessions for each, using different seeding values for the random number generator. We define as *learning curve*, the upper bound of the cumulative reward $R(\mathbf{w})$ in (2.12) obtained *at each episode* within the various training sessions. Moreover, we define as *learning variance*, the variance of the global reward between the various training sessions *at each episode*. We considered ten training sessions for all environments and for all control strategies. In the episode counting shown in the learning curves and learning variance, it is worth recalling that the BO learning initially performs 10 explorative iterations. For the GP, each iteration involves n_p episodes, with n_p the number of individuals in the population.

All the training details, i.e. the optimal weights found by the optimizers or the best tree found by the GP, are reported in the appendix.

5.1. The 0D Frequency Cross-talk problem

We here report on the results for the four algorithms for the 0D problem in Section 4.1. All implemented methods found strategies capable of solving the control problem, bringing to rest the first oscillator (s_1, s_2) while exiting the second (s_3, s_4). Table 2 collects the final best cumulative reward for each control method together with the confidence interval, defined as 1.96 time the standard deviation within the various training sessions.

The control law found by the GP yields the highest reward and the highest variance. Figures 8a and 8b show the learning curve and learning variance for the various methods.

The learning curve for the GP is initially flat because the best reward from the best individuals

$\cdot 10^{-3}$	LIPO	BO	GP	DDPG
Best Reward	-8.96 ± 0.75	-9.41 ± 1.33	-2.77 ± 1.49	-2.98 ± 1.37

Table 1: Mean optimal cost function (bold) and confidence interval (over 10 training sessions with different random number generator seeds) obtained at the end of the training for the 0D frequency cross-talk control problem.

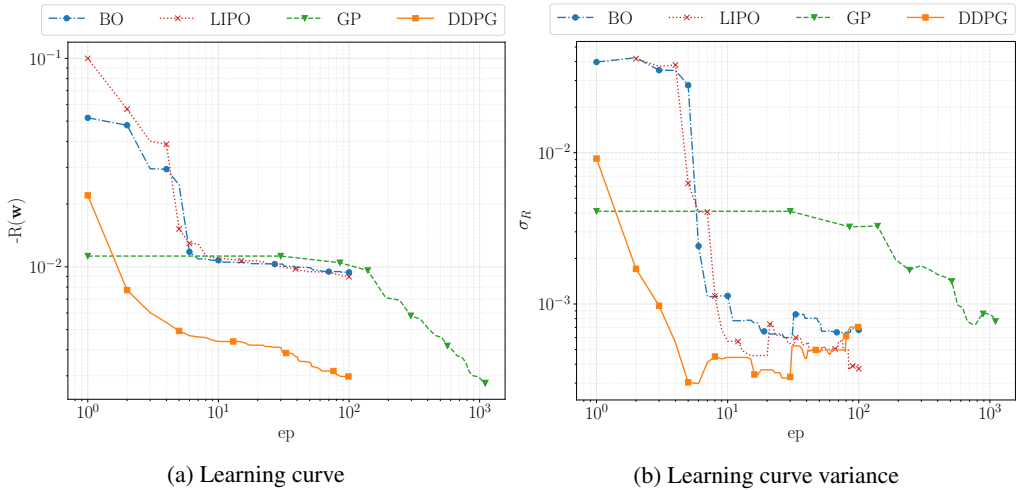


Figure 8: Comparison of the learning curves (a) and their variances (b) for different machine learning methods for the 0D test case (Sec. 4.1).

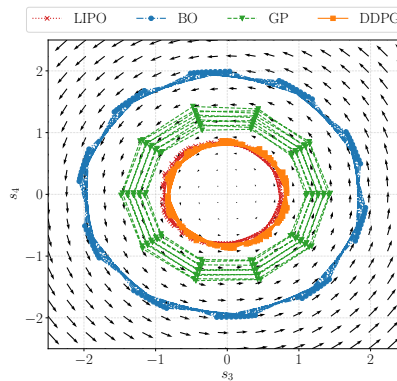


Figure 9: Orbit of the second oscillator (s_3, s_4) in the 0D control problem governed by Eq.(4.1) (left column of Fig.2) in the last part of the episode (from 194s to 200s). The coloured curves corresponds to the four control methods.

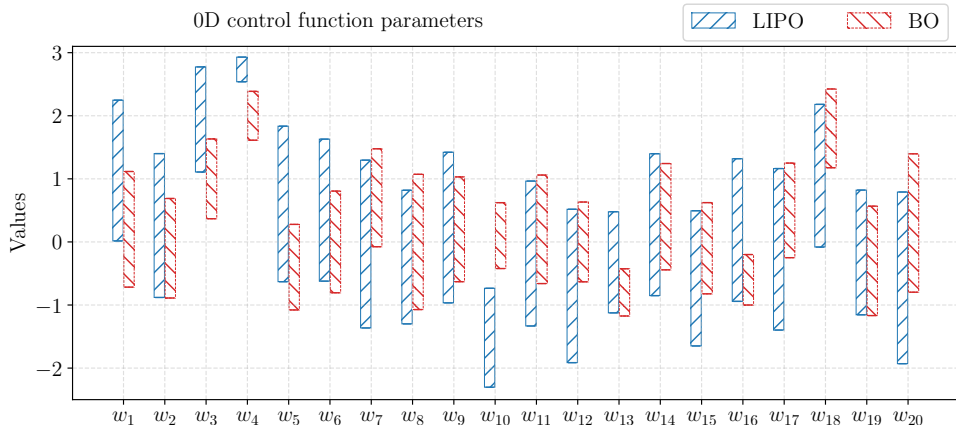


Figure 10: Weights of the control action for the 0D control problem in (10). The coloured bars represent a standard deviation around the mean value found by LIPO and BO.

of each generation is taken after all individuals have been tested. Considering that the starting population consists of 30 individuals, this shows that approximately three generations are needed before significant improvements are evident. In its simple implementation considered here, the distinctive feature of the GP is the lack of a programmatic explorative phase: exploration proceeds only through the genetic operations, and their repartition does not change over the episodes. This leads to a relatively constant (and significant) reward variance over the episodes. Possible variants to the implemented algorithms could be the reduction of the explorative operations (e.g. mutation) after various iterations (see, for example [Mendez et al. \(2021\)](#)). Nevertheless, the extensive exploration of the function space, aided by the large room for manoeuvre provided by the tree formalism, is arguably the main reason for the success of the method, which indeed finds the control law with the best cumulative reward (at the expense of a much larger number of episodes).

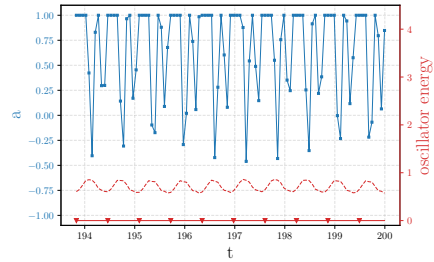
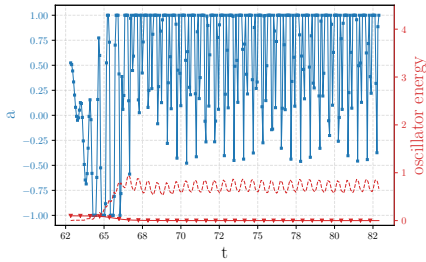
In the case of the DDPG, the steep improvement in the learning curve in the first 30 episodes might be surprising, recalling that in this phase the algorithm is still in its heavy exploratory phase (see Sec. 3.3). This trend is explained by the interplay of two factors: (1) we are showing the upper bound of the cumulative reward and (2) the effectiveness of a random search in the early training phase. Indeed, improvements over a (bad) initial choice are easily achieved by the stochastic search, while smarter updates are needed as the performances improve. This result highlights the importance of the stochastic contribution in (3.19), and its adaptation during the training to balance exploration and exploitation.

The learning behaviour of BO and LIPO is similar. Both have high variance in the early stages, as the surrogate model of the reward function is inaccurate. But both manage to obtain non-negligible improvements over the initial choice while acting randomly. The reader should notice that the variance of the LIPO at the first episode is 0 for all trainings because the initial points are always taken in the middle of the parameter space, as reported in Algorithm 2. For both methods, the learning curve steepens once the surrogate models become more accurate but reach a plateau that has surprisingly low variance after the tenth episode. This behaviour could be explained by the difficulty of both the LIPO and GP models in representing the reward function.

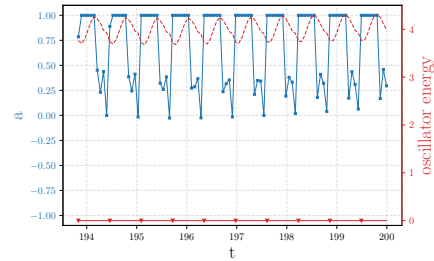
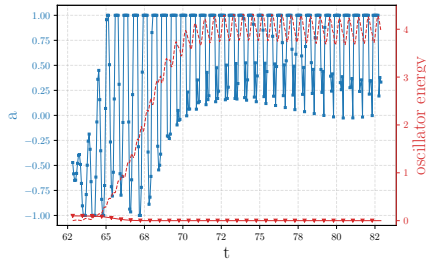
Comparing the different control strategies identified by the four methods, the main difference reside in the settling times and energy consumption. Fig. 11 shows the evolution of s_1 and s_2 from the initial conditions to the controlled configuration for each method.

As shown in Eq.(4.5), the cost function accounts mainly for the stabilization of the first oscillator and the penalization of too strong actions. In this respect, the better overall performance of the GP

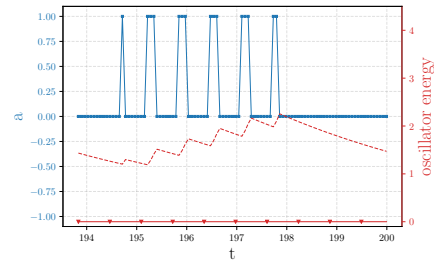
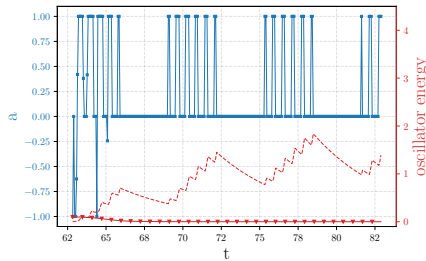
LIPO



BO



GP



DDPG

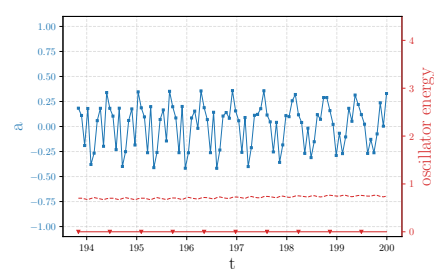
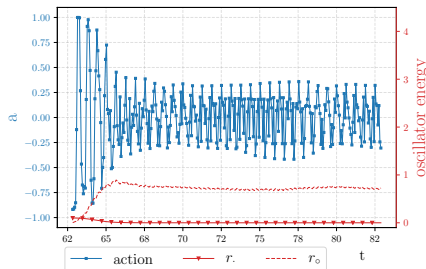


Table 2: Evolution of the best control function a (continuous blue line with squares), the energy of the first oscillator (continuous red line with triangles) and the energy of the second one (dashed red line), for the different control methods. The figures on the left report the early stage of the simulation, until the onset of a limit cycle condition, and those on the right the final time steps.

is also visible in the transitory phase of the first oscillator, shown in Fig.2, and in the evolution of the control action. These are shown in Table 2 for all the investigated algorithms. For each algorithm, the figure on the left shows the action policy and the energy E_1 (continuous red line with triangles) and E_2 (dashed red line) (see equation (4.4)) of the two oscillators in the time span

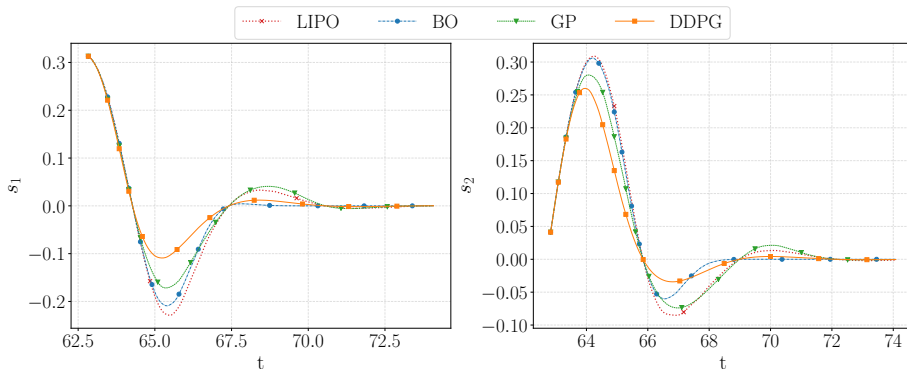


Figure 11: Evolution of the states s_1 and s_2 , associated with the unstable oscillator, obtained using the optimal control action provided by the different machine learning methods.

$t = 62 - 82$, i.e. during the early stages of the control. The figure on the right shows a zoom in the time span $t = 194 - 200$, once the system has reached a steady (controlled) state.

The control actions by LIPO and BO are qualitatively similar and results in small oscillation in the energy of the oscillator. Both sustain the second oscillator with periodic actions that saturates. The periodicity is in this case enforced by the simple quadratic law that these algorithms are called to optimize. The differences in the two strategies can be well visualized by the different choice of weights (cf. equation (4.8)), which are shown in Figure 10. While the BO systematically gives considerable importance to the weight w_{10} , which governs the quadratic response to the state s_2 , the LIPO favors a more uniform choice of weights, resulting in a limited saturation of the action and less variance. The action saturation clearly highlight the limits of the proposed quadratic control law. Both LIPO and BO give a large important to the weight w_4 because this is useful in the initial transitory to quickly energize the second oscillator. However, this term becomes a burden once the first oscillator is stabilized and forces the controller to over-react. Interestingly, simplifying the control law to the essential terms

$$a = s_1 w_1 + s_4 w_2 + s_1 s_4 w_3, \quad (5.1)$$

allows the LIPO to identify a control law with comparable performances in less than five iterations.

The GP and the DDPG use their larger model capacity to propose laws that are far more complex and more effective. The GP selects an impulsive control (also reported by Duriez *et al.* (2017)) while the DDPG proposes a periodic forcing. The impulsive strategy of the GP performs better than the DDPG (according to the metrics in 4.5) because it consumes less energy. This can be also shown by plotting the orbits of the second oscillator under the action of the four controller, as done in Figure 9. Indeed, an impulsive control is hardly described by a continuous function and this is evident from the complexity of the policy found by the GP, which reads:

$$a = \left(\log(s_2 + s_4) + e^{e^{s_4}} \right) + \frac{\sin(\log(s_2))}{\sin(\sin(\tanh(\log(-e^{(s_2^2 - s_3^2)} - s_3) \cdot (\tanh(\sin(s_1) - s_2) - s_2 s_4))))}$$

The best GP control strategy consists of two main terms. The first depends on s_2 and s_4 and the second takes all the states at the denominator and only s_2 at the numerator. This allows to moderate the control efforts once the first oscillator is stabilized.

	$\cdot 10^3$	LIPO	BO	GP	DDPG
Best Reward		-7.26 ± 0.93	-7.10 ± 0.32	-12.06 ± 12.25	-6.88 ± 0.58

Table 3: Same as table 1 but for the control of nonlinear waves in the viscous Burger’s equation.

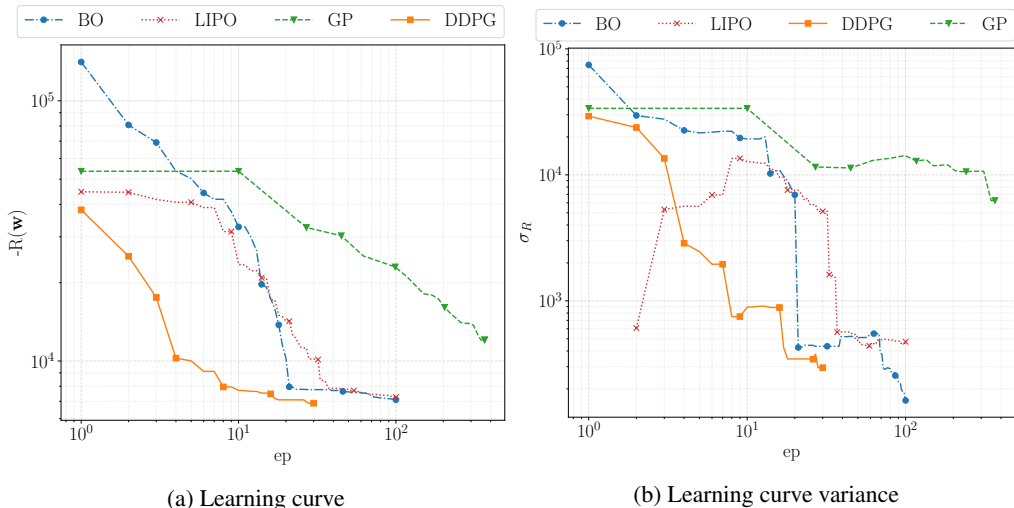


Figure 12: Comparison of the learning curves (a) and their variances (b) for different machine learning methods for the 0D test case (Sec. 4.1).

5.2. Viscous Burgers’ equation test case

We now present the results of the viscous Burgers’ test case (cf Sec.4.2). As for the previous test case, Table 3 collects the final best cumulative reward for each control method together with the confidence interval, while figures 12a and 12b show the learning curve and the learning variance over ten training sessions. The DDPG achieved the best performance, with low variance, whereas the GP performed worse in both maximum reward and variance. LIPO and BO give comparable results. For the LIPO, the learning variance initially, as the algorithm randomly selects the second and third episodes’ weights.

For this test case, the GPr-based surrogate model of the reward function used by the BO proves to be particularly successful in approximating the expected cumulative reward. This yields steep improvements in the cumulative rewards from the first iterations (recalling that the BO runs ten exploratory iterations to build its first surrogate model, which are not included in the learning curve). On the other hand, the GP does not profit from the relatively simple functional at hand and exhibits the usual stair-like learning curve since 20 were run with an initial population of 10 individuals.

The control laws found by BO and LIPO have similar weights (with differences of the order $\mathcal{O}(10^{-2})$), although the BO has much lower variance among the training sessions. Figure 13 shows the best control law derived by the four controller, together with the forcing term. These figures should be analysed together with table 4 which shows the spatio-temporal evolution of the variable $u(x,t)$ under the action of the best control law derived by the four algorithms.

The linear control laws of BO and LIPO are characterized by two main periods, one that seeks

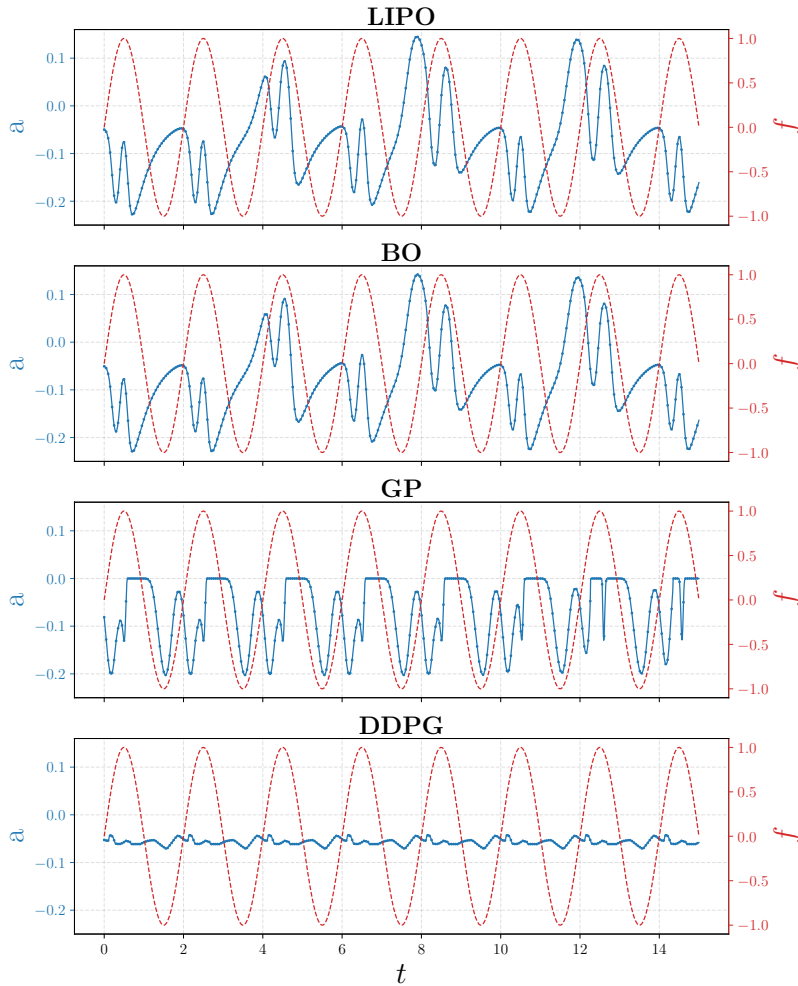


Figure 13: Comparison of the control actions derived by the four machine learning methods. The action for each control methods are shown in blue (left axis) while the curves in dashed red show the evolution of the introduced perturbation (cf. (4.11)).

to cancel the incoming wave and the second that seek to compensate the upward propagation of the control action, due to the viscous dissipation. This mechanism is clearly revealed in the spatio-temporal plots in Figure 4 for the BO and LIPO while it is moderate in the problem controlled via GP and absent in the case of the DDPG control. This mechanism challenges the closed-loop approach by the simple linear law used by the LIPO and BO because actions are fed back into the observations after a certain time. An open-loop strategy (for example introducing a constant term in the policy) could significantly ease the control task in this problem, but this option is unavailable to the LIPO and BO's linear policy used in this test. The same is true for the GP, which in this simple implementation did not have ephemeral random constant allowing for decoupling the action from the state by producing a constant action. Hinging on the nonlinearities, the GP manages nevertheless to mitigate this effects through a fairly complex action (see Table 12b) which is periodic in line with the forcing. Nevertheless towards the end of the episode, the periodicity is broken by the waves produced by the controller itself: the optimal solution analyzed

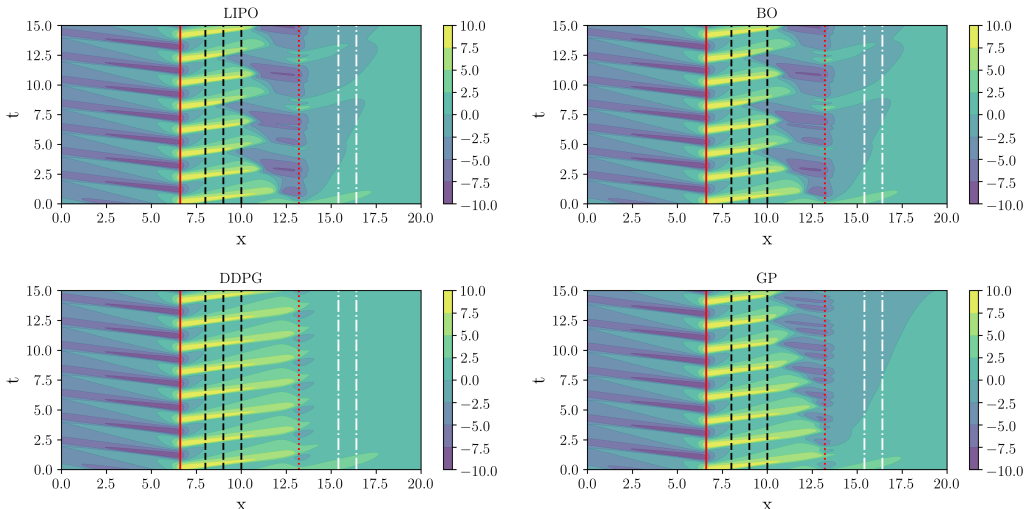


Table 4: Contour plot of the spatio-temporal evolution of u in (46) using the best control action of the different methods. The perturbation is centred at $x = 6.6$ (red continuous line) while the control law is centred at $x = 13.2$. The dashed black lines visualize the location of the observation points, while the region within the white dash-dotted line is used to evaluate the controller performance

	LIPO	BO	GP	DDPG
Best Reward	6.53 ± 0.34	6.43 ± 1.22	7.14 ± 0.86	5.58 ± 2.62

Table 5: Same as table 1 but for the von Kármán street control problem.

in this case is strongly dependent on the duration of the episode and the difficulties in dealing with the feedback of the action explains the poor performance of the GP.

The DDPG, hinging on non-linearities and the bias terms in the ANN, allows for breaking this feedback mechanics by providing an open-loop contribution such as a constant action. This strategies is particularly successful for this problem, as it allows avoiding upstream travelling (see Table 4) and leveraging more on the viscous dissipation of the system.

Nevertheless, despite the large differences in the control method and the different performances, all methods succeeds in cancelling the travelling waves. An animation of the system controlled by the four methods is provided in the supplemental material.

5.3. von Kármán street control test case

We begin the analysis of this test case with an investigation on the performances of the RL agent trained by Tang *et al.* (2020) using the Proximal Policy Optimization (PPO) on the same control problem. As recalled in section 4.3, these authors used 236 probes, located as shown in Figure 6, and a policy $\mathbf{a} = f(\mathbf{s}; \mathbf{w})$ represented by an ANN with three layers with 256 neurons each. Such a complex parametric function gives a large model capacity, and it is thus natural to analyse whether the trained agent leverage this potential model complexity.

To this end, we perform a linear regression of the policy identified by the ANN. Given $\mathbf{a} \in \mathbb{R}^4$ the action vector and $\mathbf{s} \in \mathbb{R}^{236}$ the state vector collecting information from all probes, we seek the

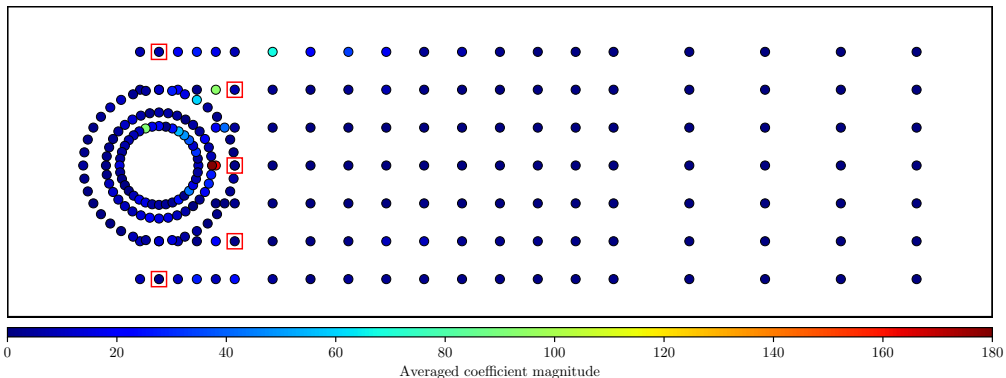


Figure 14: Scatter plot of the sensor locations, coloured by the norm of the weights $\mathbf{w}_{1j}, \mathbf{w}_{2j}, \mathbf{w}_{3j}, \mathbf{w}_{4j}$ that link the observation at state j with the action vector $\mathbf{a} = [a_1, a_2, a_3, a_4]$ in the linear regression of the policy by [Tang et al. \(2020\)](#)

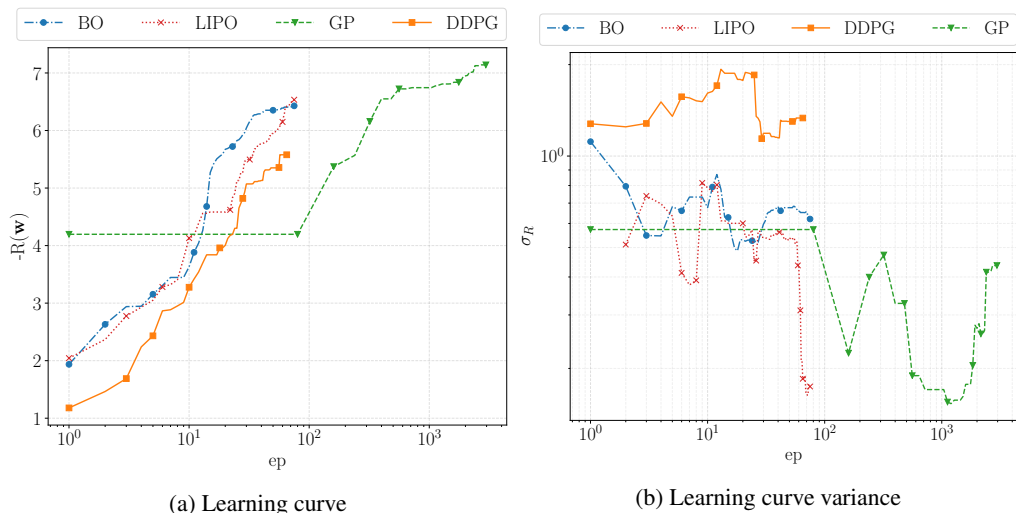


Figure 15: Comparison of the learning curves (a) and their variances (b) for different machine learning methods for the von Kármán street control problem

best linear law of the form $\mathbf{a} = \mathbf{W}\mathbf{s}$, with $\mathbf{W} \in \mathbf{R}^{4 \times 236}$ the matrix of weights of the linear policy. Let \mathbf{w}_j denote the j -th row of \mathbf{W} , hence the set of weights that linearly map the state \mathbf{s} to the action \mathbf{a}_j , i.e. the flow rate in the one of the fourth injections. One thus has $\mathbf{a}_j = \mathbf{w}_j^T \mathbf{s}$.

To perform the regression, we produce a dataset of $n_* = 400$ samples of the control law, by interrogating the ANN agent trained by [Tang et al. \(2020\)](#). Denoting as \mathbf{s}_i^* the evolution of the state i and as \mathbf{a}_i^* the vector of actions proposed by the agent the 400 samples, the linear fit of the control action is the solution of a linear least square problem, which using Ridge regression yields:

$$\mathbf{a}_j^* = \mathbf{S}\mathbf{w}_j \rightarrow \mathbf{w}_j = (\mathbf{S}^T \mathbf{S} + \alpha \mathbf{I})^{-1} \mathbf{S}^T \mathbf{a}_j^* \quad (5.2)$$

where $\mathbf{S} = [\mathbf{s}_1^*, \mathbf{s}_2^*, \dots, \mathbf{s}_{236}^*] \in \mathbf{R}^{400 \times 236}$ is the matrix collecting the 400 samples for the 236 observations along its columns, \mathbf{I} is the identity matrix of appropriate size and α is a regularization

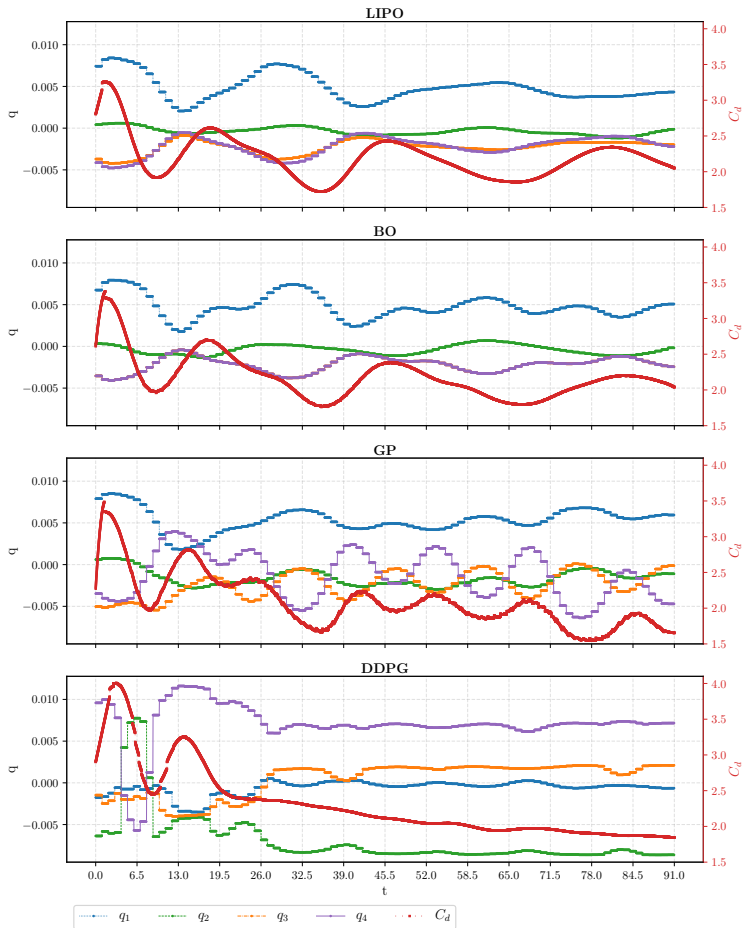


Figure 16: Evolution of the jets' flow rates(left) and the drag around the cylinder(right) for the best control action found by the different machine learning methods.

term. In this regression, the parameter α is taken running a K=5 fold validation and looking for the minima of the out-of sample error.

The result of this exercise is illuminating for two reasons. The first reason is that the residuals in the solution of (5.2) have a norm of $\|\mathbf{a}_j^* - \mathbf{S}\mathbf{w}_j\| = 1e-5$. This means that despite the large model capacity available to the ANN, the RL by Tang *et al.* (2020) is acting as a *linear controller*.

The second reason is that analysing the weights $w_{i,j} \in \mathbf{W}$, in the linearized policy $\mathbf{a}_j = \mathbf{W}\mathbf{s}$, allows for quickly identifying which of the sensors is more important in the action selection process. The result, in the form of a coloured scatter-plot, is shown in Figure 14. The markers are placed at the sensor location and coloured by the sum $\sum_i w_{i,j}^2$ for each of the j -th sensors. This result shows that only a small fraction of all the sensors play a role in the action selection. In particular, the two most important ones are placed on the rear part of the cylinder and have much larger weights than all the others.

In the light of this result with the benchmark RL agent, it becomes particularly interesting to perform the same analysis of the control action proposed by DDPG and GP, since BO and the LIPO use a linear law by construction. Figure 15a and 15b show the learning curves and learning

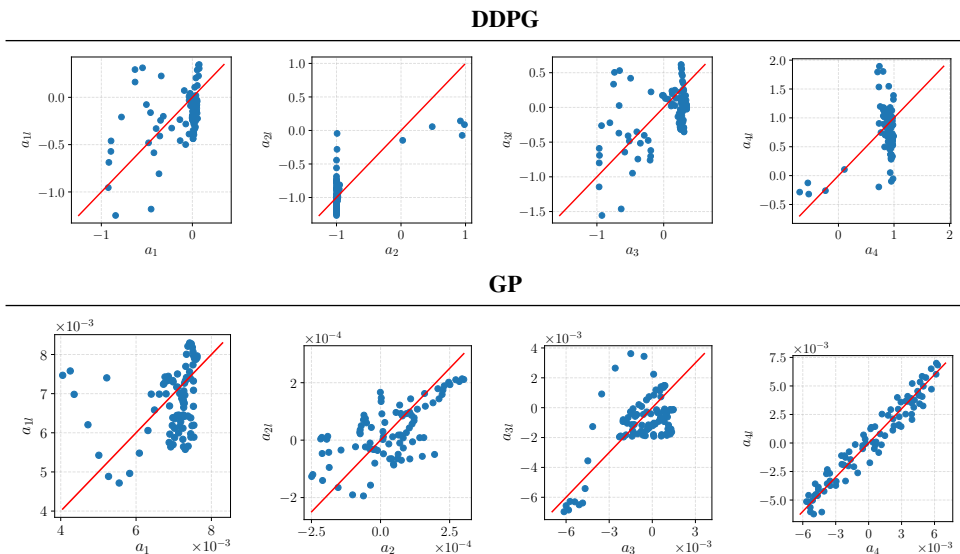


Table 6: Comparison of the optimal actions of the DDPG and GP (x axis) with their linearized version (y axis) for the four jets, the red line is the bisector of the first and third quadrant.

variance as a function of the episodes, while table 5 collects the results for the four methods in terms of the best reward and confidence interval as done for the previous test cases.

The BO and the LIPO reached an average reward of 6.43 (with the best performances of the BO hitting 7.07) in 80 episodes while the PPO agent trained by [Tang et al. \(2020\)](#) required 800 to reach a reward of 6.21, although they mainly aimed at achieving a *robust policy* across a range of Reynolds numbers. In a problem that can be well controlled by a linear policy using 5 sensors, the use of an ANN-based policy leveraging 236 sensors increases the dimensionality of the problem without benefiting from the available model capacity.

Genetic Programming had the best mean control performance with a remarkably small variance. LIPO had the lowest standard deviation due to its mainly deterministic research strategy, which selects only two random coefficients at the second and the third optimization steps.

The large exploration by the GP, on the other hand, requires more than 300 episodes to attain a better mean value than the other methods. LIPO and BO had similar trends, with an almost constant rate of improvement. This suggests that the surrogate models used in the regression are particularly effective in approximating the expected cumulative reward.

The DDPG follows a similar trend but slightly worse performances and larger variance. The large model capacity of the ANN, combined with the initial exploratory phase, tend to set the DDPG on a bad initial condition. However, this is not noticeable from the standard deviation since it is fairly low for the DDPG, which infer that the learning in the different random seeds is similar. Moreover, the DDPG presents a steep variance reduction around episode 20 due to the explorative phase's end and the exploitative start. The other methods have a lower variance which also presents peaks and valleys, but they do not have any particular trend.

Despite the low dispersion overall variance in the reward, the BO and LIPO finds largely different weights for the linear control functions, as shown in Fig. 17. This implies that fairly different strategies leads to comparable rewards. In general, the identified linear law seeks to compensate the momentum deficit due to the vortex shedding by injecting momentum with the jets on the opposite side. For example, in the case of q_4 , the LIPO gave higher weight to the observations s_2 , s_3 and s_5 which lay on the upper half-plane. The same occurs in terms of q_3 with

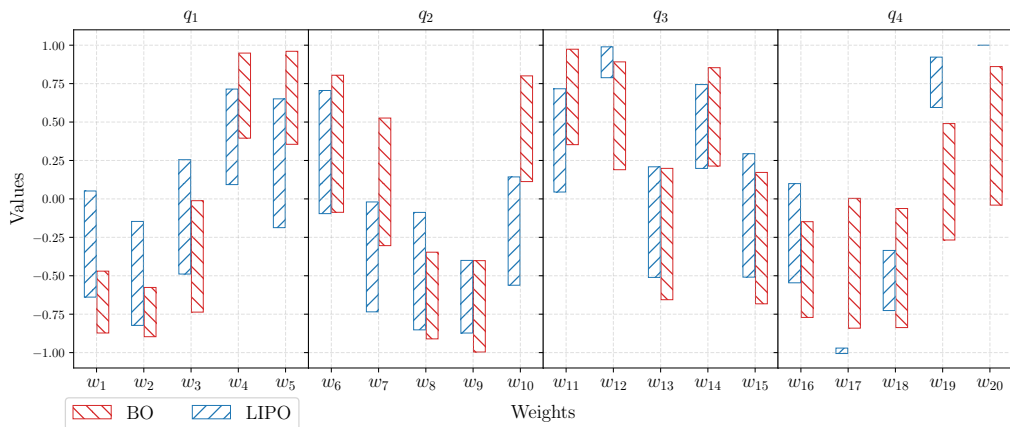


Figure 17: Weights of control action for the von Kármán street control problem, given by a linear combination of the system’s states for the four flow rates. The coloured bars represent a standard deviation around the mean value found by LIPO and BO with ten random number generator seeds.

s_2 and s_4 . To suggest that the a vortex passage in the upper part triggers the activation of the jets on the bottom part and the opposite is true in the other half-plane. Particularly interesting is the fact that neither the average weights nor their variance is symmetric with respect to the half plane.

Figure 16 show the time evolution of the four actions (flow rates) and (line red, the evolution of the instantaneous drag coefficient). Probably due to the short duration of the episode, none of the controllers identifies a symmetric control law. LIPO and BO, despite the different weights’ distribution, find an almost identical linear combination. They both produce a small flow rate for the second jet and larger flow rates for the first, both in the initial transitory and in the final stages. As the shedding is reduced and the drag coefficient drops, all flow rates tends to a constant injection for both BO and LIPO, while the GP keep continuous pulsations in both q_4 and q_3 (with opposite signs). Once again, it should be remarked that these three controllers are not allowed to act in an open loop, contrary to the DDPG.

All the control methods leads to satisfactory performances, with a mitigation of the von Kármán street and a reduction of the drag coefficient, also visible by the increased size of the recirculation bubble in the wake. The mean flow and standard deviation for the baseline and for the best strategy identified by the four techniques is shown in Figure 7. It is worth highlighting that DDPG is the only method without a symmetric distribution of the mean velocity field behind the cylinder. The vortex suppression is even more evident comparing the standard deviation of the mean velocity field with the baseline case.

Finally, we close this section by evaluating the degree of nonlinearity in the control laws derived by the GP and the DDPG. As performed for the PPO agent by [Tang et al. \(2020\)](#) at the opening of this section, we perform a linear regression with respect to the evolution of the states. The results are shown in Table 6, which compares the action taken by the DDPG (first row) and the GP (second row), in the abscissa, with the linearized actions, in the ordinate, for the four injections. None of the four injections produced by the DDPG agent can be linearized and the open-loop behaviour (constant action regardless of the states) is visible. Interestingly, the action taken by the GP on the fourth jet is almost linear.

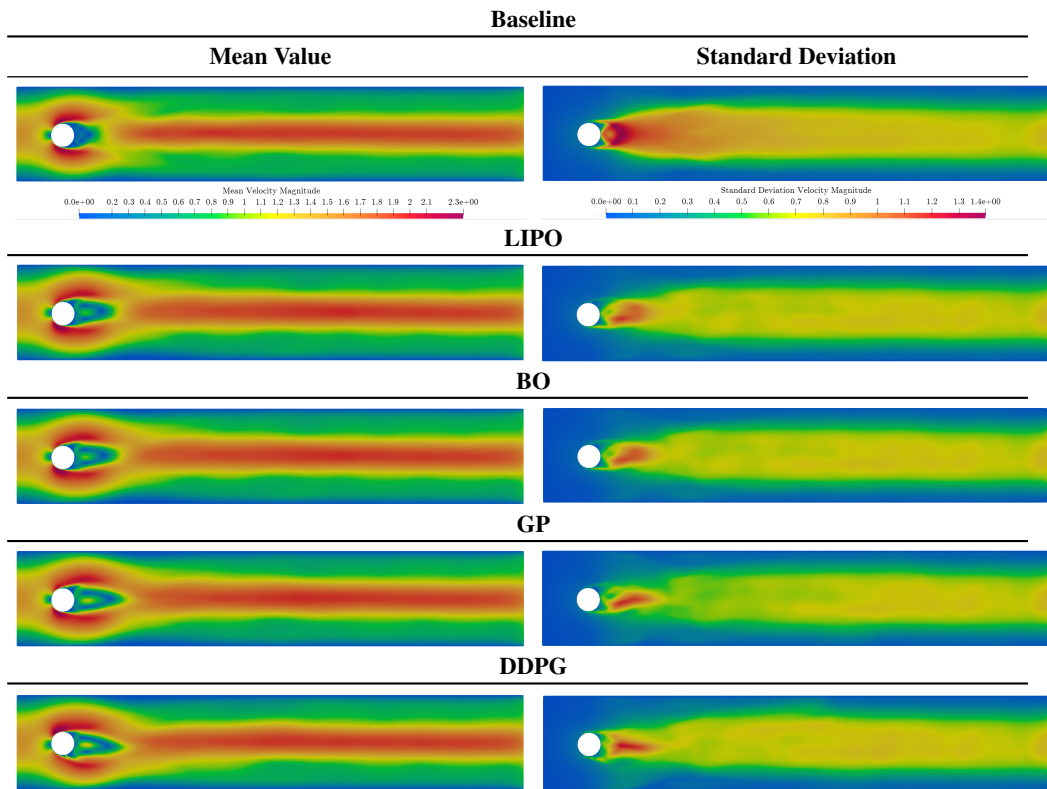


Table 7: Final pressure and velocity magnitude fields using the best control action found by the different methods.

6. Conclusions and outlooks

We presented a general mathematical framework linking machine learning-based control techniques and optimal control. The first category comprises methods based on ‘black-box optimization’ such as Bayesian Optimization (BO) and Lipschitz Global Optimization (LIPO), methods based on tree expression programming such as Genetic Programming (GP), and methods from reinforcement learning such as the Deep Deterministic Policy Gradient (DDPG).

We introduced the mathematical background for each method, in addition we illustrated their algorithmic implementation. Following the definition by [Mitchell \(1997\)](#), these algorithms *automatically* improve at a task (controlling a system) according to a performance measure (a reward function) with experience (i.e. data, collected via trial and errors from the environment). In its most classic formulation, the solution to a control problem is black-box optimization. The function to optimize measures the controller performance over a set of iterations that we call episodes. Therefore, training a controller algorithm requires (1) a function approximation to express the ‘policy’ or ‘actuation law’ linking the current state of the system to the action to take and (2) an optimizer that improves the function approximation episode after episode.

In the Bayesian Optimization and LIPO, the function approximator for the policy is defined a priori. In this work, we consider linear or quadratic controllers, but any function approximator could have been used instead (e.g. RBF or ANN). These optimizers build a surrogate model of the performance measure and adapt this model episode by episode. In Genetic Programming, the function approximator is an expression tree, and the optimization is carried out using classic evolutionary algorithms. In Reinforcement Learning (RL), particularly in the DDPG algorithm

implemented in this work, the function approximation is an ANN, and the optimizer is a stochastic (batch) gradient-based optimization. In this optimization, the gradient of the cumulative reward is computed using a surrogate model of the Q-function, i.e. the function mapping the value of each state-action pair, using a second ANN.

In the machine learning terminology, we say that the function approximators available to the GP and the DDPG have a larger ‘model capacity’ than those we used for the BO and the LIPO (linear or quadratics). This allows these algorithms to identify nonlinear control laws that are difficult to cast in the form of a prescribed parametric function. On the other hand, the larger capacity requires many learning parameters (branches and leaves in the tree expressions of the GP and weights in the ANN of the DDPG), leading to optimization problems linked to performance improvement and possible local minima. This study shows that the additional complexity does not always pay off and is sometimes unnecessary if not harmful.

We compared the ‘learning’ performances of these four algorithms on three control problems of growing complexity and dimensionality: (1) the stabilization of a nonlinear 0D oscillator, (2) the cancellation of nonlinear waves in the burgers’ equation in 1D, and (3) the drag reduction in the flow past a cylinder in laminar conditions. The successful control of these systems highlighted the strengths and weaknesses of each method, although, all algorithms identify valuable control laws in the three systems.

The GP achieve the best performances on both the stabilization of the 0D system and the control of the cylinder wake, while the DDPG gives the best performances on the control of nonlinear waves in the Burgers’ equation. However, the GP has the poorest sample efficiency in all the investigated problems, thus requiring a larger number of interactions with the system, and has the highest learning variance, meaning that repeating the training leads to vastly different results. This behaviour is inherent to the population-based and evolutionary optimization algorithm, which has the main merit of escaping local minima in problems characterized by complex functionals. These features paid off in the 0D problem, for which the GP derives an effective impulsive policy, but are ineffective in the control of nonlinear waves in the Burgers’ equation, characterized by a much simpler reward functional.

On the other side of the spectra in terms of sample efficiency are the black box optimizers such as LIPO and BO. Their performance is strictly dependent on the effectiveness of the predetermined policy parametrization to optimize. In the case of the 0D control problem, the quadratic policy is, in its simplicity, less effective than the complex policy derived by GP and DDPG. However, in the nonlinear wave cancellation problem, the only limit was the lack of a constant (open-loop) term. For the problem of drag reduction in the cylinder flow, the linear policy was rather satisfactory. To the point that it was shown that the PPO policy by [Tang et al. \(2020\)](#) has, in fact, derived a linear policy. The DDPG implemek was trained using 5 sensors (instead of 236) and reached a performance comparable to the PPO by [Tang et al. \(2020\)](#) in 80 episodes (instead of 800). Nevertheless, although the policy derived by the DDPG is nonlinear, its performances are comparable to the linear laws derived by BO and LIPO. Yet, the policy by the DDPG is based on an ANN parametrized by 68361 parameters (4 fully connected layers with 5 neurons in the first, 256 in the second and third and 4 in the output) while the linear laws used by BO and LIPO only depend on 5 parameters.

We believe that this work has shed some light (or open some paths) on two main aspects of the machine-learning-based control problem: (1) the contrast between the generality of the function approximator for the policy and the number of episodes required to obtain good control actions; (2) the need for tailoring the model complexity to control task at hand and the possibility of having a modular approach in the construction of the optimal control law. The resolution of both aspects resides in the hybridization of the investigated methods.

Concerning the choice of the function approximator (or more generally the policy parametrization, or the ‘hypothesis set’ in the machine learning terminology), both ANN and expression

offer large modelling capacities, with the seconds often outperforming the first in the author's experience. Intermediate solutions such as RBFs or Gaussian processes can provide a valid compromise between model capacity and dimensionality of their parameter space. They should be explored more in the field of flow control.

Finally, concerning the dilemma model complexity versus task complexity, a possible solution could be increasing the complexity modularly. For example, one could limit the function space in the GP by first taking linear functions and then enlarging it modularly, adding more primitives. Or, in a hybrid formalism, one could first train a linear or polynomial controller (e.g. via LIPO or BO) and then use it to pre-train models of larger complexity (e.g. ANNs or expression trees) in a supervised fashion, or to assist their training with the environment (for instance by inflating the replay buffer of the DDPG with transitions learned by the BO/LIPO models).

This is the essence of 'behavioural cloning', in which a first agent (called 'demonstrator') trains a second one (called 'imitator') offline so that the second does not start from scratch. This is unexplored territory in flow control and, of course, opens the question of how much the supervised training phase should last and whether the pupil could ever surpass the master.

Appendix A. From Hamilton-Jacobi-Bellman to the adjoint differential equation

Starting from the HJB equation in (2.10):

$$\partial_t V^*(\mathbf{s}, t) + \max_{\mathbf{a} \in \mathcal{A}} \left\{ \mathcal{L}(\mathbf{s}, \mathbf{a}, t) + \partial_{\mathbf{s}} V(\mathbf{s}, t) \mathbf{f}(\mathbf{s}, \mathbf{a}, t) \right\} = 0, \quad (\text{A } 1)$$

assume $\mathbf{a}^*(t)$ is the optimal control function. This leads to:

$$\partial_t V^*(\mathbf{s}, t) + \mathcal{L}(\mathbf{s}, \mathbf{a}^*, t) + \partial_{\mathbf{s}} V(\mathbf{s}, t) \mathbf{f}(\mathbf{s}, \mathbf{a}^*, t) = 0. \quad (\text{A } 2)$$

Differentiating both sides with respect to the state vector \mathbf{s} :

$$\partial_{\mathbf{s}} \partial_t V^*(\mathbf{s}, t) + \partial_{\mathbf{s}} \mathcal{L}(\mathbf{s}, \mathbf{a}^*, t) + \partial_{\mathbf{s}} \left[\partial_{\mathbf{s}} V(\mathbf{s}, t) \mathbf{f}(\mathbf{s}, \mathbf{a}^*, t) \right] = 0, \quad (\text{A } 3)$$

and using the product rule, yields:

$$\partial_{t\mathbf{s}} V^*(\mathbf{s}, t) + \partial_{\mathbf{s}} \mathcal{L}(\mathbf{s}, \mathbf{a}^*, t) + \partial_{\mathbf{s}^2} V(\mathbf{s}, t) \mathbf{f}(\mathbf{s}, \mathbf{a}^*, t) + \quad (\text{A } 4)$$

$$+ \partial_{\mathbf{s}} V(\mathbf{s}, t) \partial_{\mathbf{s}} \mathbf{f}(\mathbf{s}, \mathbf{a}^*, t) = 0. \quad (\text{A } 5)$$

Rearranging terms:

$$\partial_{t\mathbf{s}} V^*(\mathbf{s}, t) + \partial_{\mathbf{s}^2} V(\mathbf{s}, t) \mathbf{f}(\mathbf{s}, \mathbf{a}^*, t) = \quad (\text{A } 6)$$

$$= -\partial_{\mathbf{s}} \mathcal{L}(\mathbf{s}, \mathbf{a}^*, t) - \partial_{\mathbf{s}} V(\mathbf{s}, t) \partial_{\mathbf{s}} \mathbf{f}(\mathbf{s}, \mathbf{a}^*, t), \quad (\text{A } 7)$$

where:

$$\begin{aligned} \partial_t \left[\partial_{\mathbf{s}} V(\mathbf{s}, t) \right] &= \partial_{t\mathbf{s}} V^*(\mathbf{s}, t) + \partial_{\mathbf{s}^2} V(\mathbf{s}, t) \dot{\mathbf{s}} \\ &= \partial_{t\mathbf{s}} V^*(\mathbf{s}, t) + \partial_{\mathbf{s}^2} V(\mathbf{s}, t) \mathbf{f}(\mathbf{s}, \mathbf{a}^*, t). \end{aligned} \quad (\text{A } 8)$$

Then:

$$\partial_t \left[\partial_{\mathbf{s}} V(\mathbf{s}, t) \right] = -\partial_{\mathbf{s}} \mathcal{L}(\mathbf{s}, \mathbf{a}^*, t) - \partial_{\mathbf{s}} V(\mathbf{s}, t) \partial_{\mathbf{s}} \mathbf{f}(\mathbf{s}, \mathbf{a}^*, t). \quad (\text{A } 9)$$

Noticing that this is true for any \mathbf{s} that solves the HJB equation, it must also be true for the optimal trajectory \mathbf{s}^* associated with the optimal control action \mathbf{a}^*

$$\partial_t \left[\partial_{\mathbf{s}} V(\mathbf{s}^*, t) \right] = -\partial_{\mathbf{s}} \mathcal{L}(\mathbf{s}^*, \mathbf{a}^*, t) - \partial_{\mathbf{s}} V(\mathbf{s}^*, t) \partial_{\mathbf{s}} \mathbf{f}(\mathbf{s}^*, \mathbf{a}^*, t), \quad (\text{A } 10)$$

which yields the classical result of the max principle presented in Eq.(2.6)

$$\partial_t \lambda(t) = -\partial_{\mathbf{s}} \mathcal{L}(\mathbf{s}^*, \mathbf{a}^*, t) - \underbrace{\partial_{\mathbf{s}} V(\mathbf{s}^*, t)}_{\lambda(t)} \partial_{\mathbf{s}} \mathbf{f}(\mathbf{s}^*, \mathbf{a}^*, t), \quad (\text{A } 11)$$

somewhat magically the $\lambda(t)$ no longer depends on the states \mathbf{s} as it did in the HJB, so the right-hand side is in fact the partial derivative of the Hamiltonian with respect to \mathbf{s} .

Appendix B. Weights identified by the BO and LIPO

The tables below collect the weights for the linear and nonlinear policies identified by LIPO and BO for the three investigated control problems. The reported value represents the mean of ten optimizations with different random conditions and the uncertainty is taken as the standard deviation.

	w1	w2	w3	w4	w5	w6	w7	w8	w9	w10
LIPO	1.13 ± 2.23	0.26 ± 2.28	1.94 ± 1.67	2.73 ± 0.39	0.6 ± 2.47	0.5 ± 2.25	-0.03 ± 2.66	-0.24 ± 2.12	0.23 ± 2.39	-1.52 ± 1.57
BO	0.2 ± 1.83	-0.1 ± 1.58	1 ± 1.26	2 ± 0.77	-0.4 ± 1.36	0 ± 1.61	0.7 ± 1.55	0 ± 2.14	0.2 ± 1.66	0.1 ± 1.04
	w11	w12	w13	w14	w15	w16	w17	w18	w19	w20
LIPO	-0.18 ± 2.3	-0.7 ± 2.43	-0.32 ± 1.6	0.27 ± 2.25	-0.58 ± 2.14	0.19 ± 2.26	-0.12 ± 2.56	1.05 ± 2.26	-0.17 ± 1.98	-0.57 ± 2.72
BO	0.2 ± 1.72	0 ± 1.26	-0.8 ± 0.75	0.4 ± 1.69	-0.1 ± 1.45	-0.6 ± 0.8	0.5 ± 1.5	1.8 ± 1.25	-0.3 ± 1.73	0.3 ± 2.19

Table 8: Mean value and half standard deviation of the 0D feedback control law coefficients

	w1	w2	w3
LIPO	-0.02(± 0.01)	0.03(± 0.03)	-0.03(± 0.02)
BO	-0.02(± 0.00)	0.02(± 0.01)	-0.03(± 0.00)

Table 9: Mean value and half standard deviation of the Burgers' feedback control law coefficients

	w1	w2	w3	w4	w5	w6	w7	w8	w9	w10
LIPO	-0.29 ± 0.69	-0.48 ± 0.67	-0.12 ± 0.74	0.40 ± 0.62	0.23 ± 0.84	0.30 ± 0.80	-0.38 ± 0.71	-0.47 ± 0.76	-0.64 ± 0.47	-0.21 ± 0.70
BO	-0.67 ± 0.40	-0.73 ± 0.32	-0.37 ± 0.72	0.67 ± 0.55	0.66 ± 0.60	0.36 ± 0.89	0.11 ± 0.83	-0.63 ± 0.56	0.7 ± 0.59	0.46 ± 0.69
	w11	w12	w13	w14	w15	w16	w17	w18	w19	w20
LIPO	0.38 ± 0.67	0.89 ± 0.2	-0.15 ± 0.72	0.47 ± 0.55	-0.11 ± 0.80	-0.22 ± 0.65	-0.99 ± 0.04	-0.53 ± 0.39	0.76 ± 0.32	1.0 ± 0.0
BO	0.66 ± 0.62	0.54 ± 0.7	-0.23 ± 0.85	0.53 ± 0.64	-0.26 ± 0.85	-0.46 ± 0.62	-0.42 ± 0.84	-0.45 ± 0.77	0.11 ± 0.76	0.41 ± 0.90

Table 10: Mean value and half standard deviation of the von Karman vortex street feedback control law coefficients

REFERENCES

- ABU-MOSTAFA, YASER S., MAGDON-ISMAIL, MALIK & LIN, HSUAN-TIEN 2012 *Learning from Data*. AMLBook.
- AHMED, MOHAMED OSAMA, VASWANI, SHARAN & SCHMIDT, MARK 2020 Combining bayesian optimization and lipschitz optimization. *Machine Learning* **109** (1), 79–102.
- ALEKSIC, KATARINA, LUCHTENBURG, MARK, KING, RUDIBERT, NOACK, BERND & PFEIFER, JENS 2010 Robust nonlinear control versus linear model predictive control of a bluff body wake. In *5th Flow Control Conference*. American Institute of Aeronautics and Astronautics.
- ALNÆS, MARTIN, BLECHTA, JAN, HAKE, JOHAN, JOHANSSON, AUGUST, KEHLET, BENJAMIN, LOGG, ANDERS, RICHARDSON, CHRIS, RING, JOHANNES, ROGNES, MARIE E & WELLS, GARTH N 2015 The fenics project version 1.5. *Archive of Numerical Software* **3** (100).
- APATA, O & OYEDOKUN, DTO 2020 An overview of control techniques for wind turbine systems. *Scientific African* p. e00566.
- ARCHETTI, FRANCESCO & CANDELIERI, ANTONIO 2019 *Bayesian optimization and data science*. Springer.
- BACK, FOGEL & MICHALEWICZ 2000 *Evolutionary Computation 1 : Basic Algorithms and Operators*.
- BALABANE, MIKHAEL, MENDEZ, MIGUEL ALFONSO & NAJEM, SARA 2021 Koopman operator for burgers's equation. *Physical Review Fluids* **6** (6).
- BANZHAF, WOLFGANG, NORDIN, PETER & KELLER, ROBERT E. 1997 *Genetic Programming: An Introduction*. MORGAN KAUFMANN PUBL INC.
- BAZARAA, MOKHTAR S., SHERALI, HANIF D. & SHETTY, C. M. 2005 *Nonlinear Programming*. John Wiley & Sons, Inc.
- BEINTEMA, GERBEN, CORBETTA, ALESSANDRO, BIFERALE, LUCA & TOSCHI, FEDERICO 2020 Controlling rayleigh-bénard convection via reinforcement learning. *Journal of Turbulence* **21** (9-10), 585–605.
- BELUS, VINCENT, RABAULT, JEAN, VIQUERAT, JONATHAN, CHE, ZHIZHAO, HACHEM, ELIE & REGLADE, ULYSSE 2019 Exploiting locality and physical invariants to design effective deep reinforcement learning control of the unstable falling liquid film. *arXiv preprint arXiv:1910.07788*.
- BENARD, N., PONS-PRATS, J., PERIAUX, J., BUGEDA, G., BRAUD, P., BONNET, J. P. & MOREAU, E. 2016 Turbulent separated shear flow control by surface plasma actuator: experimental optimization by genetic algorithm approach. *Experiments in Fluids* **57** (2).
- BERGMANN, MICHEL, CORDIER, LAURENT & BRANCHER, JEAN-PIERRE 2005 Optimal rotary control of the cylinder wake using proper orthogonal decomposition reduced-order model. *Physics of Fluids* **17** (9), 097101.
- BERGSTRA, J., YAMINS, DANIEL & COX, D. 2013 Making a science of model search: Hyperparameter optimization in hundreds of dimensions for vision architectures. In *ICML*.
- BERSINI, H. & GORRINI, V. 1996 Three connectionist implementations of dynamic programming for optimal control: a preliminary comparative analysis. IEEE Comput. Soc. Press.
- BEWLEY, THOMAS R 2001 Flow control: new challenges for a new renaissance. *Progress in Aerospace sciences* **37** (1), 21–58.
- BEWLEY, THOMAS R., MOIN, PARVIZ & TEMAM, ROGER 2001 DNS-based predictive control of turbulence: an optimal benchmark for feedback algorithms. *Journal of Fluid Mechanics* **447**, 179–225.
- BEYER, HANS-GEORG & SCHWEFEL, HANS-PAUL 2002 Evolution strategies - a comprehensive introduction. *Natural Computing* **1**, 3–52.
- BIRAL, FRANCESCO, BERTOLAZZI, ENRICO & BOSETTI, PAOLO 2016 Notes on numerical methods for solving optimal control problems. *IEEJ Journal of Industry Applications* **5** (2), 154–166.
- BLANCHARD, ANTOINE B, CORNEJO MACEDA, GUY Y, FAN, DEWEI, LI, YIQING, ZHOU, YU, NOACK, BERND R & SAPSIS, THEMISTOKLIS P 2022 Bayesian optimization for active flow control. *Acta Mechanica Sinica* pp. 1–13.
- BÖHME, THOMAS J & FRANK, BENJAMIN 2017 Direct methods for optimal control. In *Hybrid Systems, Optimal Control and Hybrid Vehicles*, pp. 233–273. Springer.
- BRUNTON, S. 2009 *Methods for System Identification*. AIAA.
- BRUNTON, S. 2022 *Methods for System Identification*. Cambridge University Press.
- BRUNTON, STEVEN L. & NOACK, BERND R. 2015 Closed-loop turbulence control: Progress and challenges. *Applied Mechanics Reviews* **67** (5).

- BRUNTON, STEVEN L, NOACK, BERND R & KOUMOUTSAKOS, PETROS 2020 Machine learning for fluid mechanics. *Annual Review of Fluid Mechanics* **52**, 477–508.
- BUCCI, MICHELE ALESSANDRO, SEMERARO, ONOFRIO, ALLAUZEN, ALEXANDRE, WISNIEWSKI, GUILLAUME, CORDIER, LAURENT & MATHELIN, LIONEL 2019 Control of chaotic systems by deep reinforcement learning. *Proceedings of the Royal Society A* **475** (2231), 20190351.
- CARNARIUS, ANGELO, THIELE, FRANK, OEZKAYA, EMRE & GAUGER, NICOLAS R 2010 Adjoint approaches for optimal flow control. In *5th Flow Control Conference*, p. 5088.
- COLLIS, S.S., GHAYOUR, K. & HEINKENSCHLOSS, M. 2002 Optimal control of aeroacoustic noise generated by cylinder vortex interaction. *International Journal of Aeroacoustics* **1** (2), 97–114.
- DAVIDSON, KENNETH R & DONSIG, ALLAN P 2009 *Real analysis and applications: theory in practice*. Springer Science & Business Media, pg. 70.
- DEBIEN, ANTOINE, VON KRBEK, KAI A. F. F., MAZELLIER, NICOLAS, DURIEZ, THOMAS, CORDIER, LAURENT, NOACK, BERND R., ABEL, MARKUS W. & KOURTA, AZEDDINE 2016 Closed-loop separation control over a sharp edge ramp using genetic programming. *Experiments in Fluids* **57** (3).
- DELPORT, S., BAELEMANS, M. & MEYERS, J. 2011 Maximizing dissipation in a turbulent shear flow by optimal control of its initial state. *Physics of Fluids* **23** (4), 045105.
- DIRK, M. LUCHTENBURG, GÜNTHER, BERT, NOACK, BERND R., KING, RUDIBERT & TADMOR, GILEAD 2009 A generalized mean-field model of the natural and high-frequency actuated flow around a high-lift configuration. *Journal of Fluid Mechanics* **623**, 283–316.
- DURIEZ, THOMAS, BRUNTON, STEVEN L & NOACK, BERND R 2017 *Machine learning control-taming nonlinear dynamics and turbulence*. Springer.
- EVANS, LAWRENCE C. 1983 An introduction to mathematical optimal control theory, lecture notes.
- FAN, DIXIA, YANG, LIU, WANG, ZHICHENG, TRIANTAFYLLOU, MICHAEL S. & KARNIADAKIS, GEORGE EM 2020 Reinforcement learning for bluff body active flow control in experiments and simulations. *Proceedings of the National Academy of Sciences* **117** (42), 26091–26098.
- FASSHAUER, GREGORY E 2007 *Meshfree Approximation Methods with Matlab*. WORLD SCIENTIFIC.
- FLEMING, PETER J & FONSECA, CARLOS M 1993 Genetic algorithms in control systems engineering. *IFAC Proceedings Volumes* **26** (2), 605–612.
- FLINOIS, THIBAUT L. B. & COLONIUS, TIM 2015 Optimal control of circular cylinder wakes using long control horizons. *Physics of Fluids* **27** (8), 087105.
- FORRESTER, ALEXANDER I. J., SÓBESTER, ANDRÁS & KEANE, ANDY J. 2008 *Engineering Design via Surrogate Modelling*. Wiley.
- FORTIN, FÉLIX-ANTOINE, DE RAINVILLE, FRANÇOIS-MICHEL, GARDNER, MARC-ANDRÉ, PARIZEAU, MARC & GAGNÉ, CHRISTIAN 2012 DEAP: Evolutionary algorithms made easy. *Journal of Machine Learning Research* **13**, 2171–2175.
- FRAZIER, PETER I. 2018 A tutorial on bayesian optimization , arXiv: <http://arxiv.org/abs/1807.02811v1>.
- FUJIMOTO, SCOTT, VAN HOOF, HERKE & MEGER, DAVID 2018 Addressing function approximation error in actor-critic methods , arXiv: <http://arxiv.org/abs/1802.09477v3>.
- GARNIER, PAUL, VIQUERAT, JONATHAN, RABAULT, JEAN, LARCHER, AURÉLIEN, KUHNLE, ALEXANDER & HACHEM, ELIE 2021 A review on deep reinforcement learning for fluid mechanics. *Computers & Fluids* **225**, 104973.
- GAUTIER, N., AIDER, J.-L., DURIEZ, T., NOACK, B. R., SEGOND, M. & ABEL, M. 2015 Closed-loop separation control using machine learning. *Journal of Fluid Mechanics* **770**, 442–457.
- GAZZOLA, MATTIA, HEJAZIALHOSSEINI, BABAK & KOUMOUTSAKOS, PETROS 2014 Reinforcement learning and wavelet adapted vortex methods for simulations of self-propelled swimmers. *SIAM Journal on Scientific Computing* **36** (3), B622–B639.
- GHAVAMZADEH, MOHAMMED, MANNOR, SHIE, PINEAU, JOELLE & TAMAR, AVIV 2015 Convex optimization: Algorithms and complexity. *Foundations and Trends® in Machine Learning* **8** (5-6), 359–483.
- GOODFELLOW, IAN, BENGIO, YOSHUA & COURVILLE, AARON 2016 *Deep Learning*. the MIT Press.
- GUNZBURGER, MAX D. 2002 *Perspectives in Flow Control and Optimization*. Society for Industrial and Applied Mathematics.
- EL HAK, MOHAMED GAD 2000 *Flow Control*. Cambridge University Press.
- HAUPT, RANDY L & ELLEN HAUPT, SUE 2004 *Practical genetic algorithms* .
- HEAD, TIM, KUMAR, MANOJ, NAHRSTAEDT, HOLGER, LOUPPE, GILLES & SHCHERBATYI, IAROSLAV 2020 scikit-optimize/scikit-optimize.

- JIN, BO, ILLINGWORTH, SIMON J. & SANDBERG, RICHARD D. 2020 Feedback control of vortex shedding using a resolvent-based modelling approach. *Journal of Fluid Mechanics* **897**.
- JONES, DONALD R., SCHONLAU, MATTHIAS & WELCH, WILLIAM J. 1998 *Journal of Global Optimization* **13** (4), 455–492.
- KELLEY, HENRY J 1960 Gradient theory of optimal flight paths. *Ars Journal* **30** (10), 947–954.
- KIM, JOHN & BEWLEY, THOMAS R. 2007 A linear systems approach to flow control. *Annual Review of Fluid Mechanics* **39** (1), 383–417.
- KIM, JEONGLAE, BODONY, DANIEL J. & FREUND, JONATHAN B. 2014 Adjoint-based control of loud events in a turbulent jet. *Journal of Fluid Mechanics* **741**, 28–59.
- KING, DAVIS E. 2009 Dlib-ml: A machine learning toolkit. *Journal of Machine Learning Research* **10**, 1755–1758.
- KIRK, DONALD E 2004 *Optimal control theory: an introduction*. Courier Corporation.
- KOBER, JENS & PETERS, JAN 2014 Reinforcement learning in robotics: A survey. In *Springer Tracts in Advanced Robotics*, pp. 9–67. Springer International Publishing.
- KOZA, JOHN R. 1994 Genetic programming as a means for programming computers by natural selection. *Statistics and Computing* **4** (2).
- KRAFT, DIETER 1985 On converting optimal control problems into nonlinear programming problems. In *Computational Mathematical Programming*, pp. 261–280. Springer Berlin Heidelberg.
- LANG, WALTER, POINSOT, THIERRY & CANDEL, SEBASTIEN 1987 Active control of combustion instability. *Combustion and Flame* **70** (3), 281–289.
- LEE, CHANGHOON, KIM, JOHN, BABCOCK, DAVID & GOODMAN, RODNEY 1997 Application of neural networks to turbulence control for drag reduction. *Physics of Fluids* **9** (6), 1740–1747.
- LI, JICHAO & ZHANG, MENGQI 2021 Reinforcement-learning-based control of confined cylinder wakes with stability analyses. *Journal of Fluid Mechanics* **932**.
- LI, RUIYING, NOACK, BERND R., CORDIER, LAURENT, BORÉE, JACQUES & HARAMBAT, FABIEN 2017 Drag reduction of a car model by linear genetic programming control. *Experiments in Fluids* **58** (8).
- LI, YIQING, CUI, WENSHI, JIA, QING, LI, QILIANG, YANG, ZHIGANG, MORZYŃSKI, MAREK & NOACK, BERND R. 2019 Explorative gradient method for active drag reduction of the fluidic pinball and slanted ahmed body , arXiv: <http://arxiv.org/abs/1905.12036v2>.
- LILLICRAP, TIMOTHY P., HUNT, JONATHAN J., PRITZEL, ALEXANDER, HEES, NICOLAS, EREZ, TOM, TASSA, YUVAL, SILVER, DAVID & WIERSTRA, DAAN 2015 Continuous control with deep reinforcement learning , arXiv: <http://arxiv.org/abs/1509.02971v6>.
- LIN, JOHN C 2002 Review of research on low-profile vortex generators to control boundary-layer separation. *Progress in Aerospace Sciences* **38** (4-5), 389–420.
- LONGUSKI, JAMES M, GUZMÁN, JOSÉ J. & PRUSSING, JOHN E. 2014 *Optimal Control with Aerospace Applications*. Springer New York.
- LUKETINA, JELENA, NARDELLI, NANTAS, FARQUHAR, GREGORY, FOERSTER, JAKOB, ANDREAS, JACOB, GREFENSTETTE, EDWARD, WHITESON, SHIMON & ROCKTÄSCHEL, TIM 2019 A survey of reinforcement learning informed by natural language , arXiv: <http://arxiv.org/abs/1906.03926v1>.
- MACEDA, GUY Y. CORNEJO, LI, YIQING, LUSSEYRAN, FRANÇOIS, MORZYŃSKI, MAREK & NOACK, BERND R. 2021 Stabilization of the fluidic pinball with gradient-enriched machine learning control. *Journal of Fluid Mechanics* **917**.
- MACEDA, GUY YOSLAN CORNEJO, NOACK, BERND R, LUSSEYRAN, FRANÇOIS, MORZYŃSKI, MAREK, PASTUR, LUC & DENG, NAN 2018 Taming the fluidic pinball with artificial intelligence control. In *European Fluid Mechanics Conference*.
- MAHFOZE, OA, MOODY, A, WYNN, A, WHALLEY, RD & LAIZET, S 2019 Reducing the skin-friction drag of a turbulent boundary-layer flow with low-amplitude wall-normal blowing within a bayesian optimization framework. *Physical Review Fluids* **4** (9), 094601.
- MALHERBE, CÉDRIC & VAYATIS, NICOLAS 2017 Global optimization of lipschitz functions. In *International Conference on Machine Learning*, pp. 2314–2323. PMLR.
- MELIGA, PHILIPPE, SIPP, DENIS & CHOMAZ, JEAN-MARC 2010 Open-loop control of compressible afterbody flows using adjoint methods. *Physics of Fluids* **22** (5), 054109.
- MENDEZ, FRANCISCO JOSÉ, PASCULLI, ANTONIO, MENDEZ, MIGUEL ALFONSO & SCIARRA, NICOLA 2021 Calibration of a hypoplastic model using genetic algorithms. *Acta Geotechnica* **16** (7), 2031–2047.
- MITCHELL, TOM 1997 *Machine Learning*. New York: McGraw-Hill.
- MNIH, VOLODYMYR, KAVUKCUOGLU, KORAY, SILVER, DAVID, GRAVES, ALEX, ANTONOGLU,

- IOANNIS, WIERSTRA, DAAN & RIEDMILLER, MARTIN 2013 Playing atari with deep reinforcement learning , arXiv: <http://arxiv.org/abs/1312.5602v1>.
- MNIH, VOLODYMYR, KAVUKCUOGLU, KORAY, SILVER, DAVID, RUSU, ANDREI A., VENESS, JOEL, BELLEMARE, MARC G., GRAVES, ALEX, RIEDMILLER, MARTIN, FIDJELAND, ANDREAS K., OSTROVSKI, GEORG, PETERSEN, STIG, BEATTIE, CHARLES, SADIK, AMIR, ANTONOGLU, IOANNIS, KING, HELEN, KUMARAN, DHARSHAN, WIERSTRA, DAAN, LEGG, SHANE & HASSABIS, DEMIS 2015 Human-level control through deep reinforcement learning. *Nature* **518** (7540), 529–533.
- MUNTERS, WIM & MEYERS, JOHAN 2018 Dynamic strategies for yaw and induction control of wind farms based on large-eddy simulation and optimization. *Energies* **11** (1), 177.
- NIAN, RUI, LIU, JINFENG & HUANG, BIAO 2020 A review on reinforcement learning: Introduction and applications in industrial process control **139**, 106886.
- NITA, C., VANDEWALLE, S. & MEYERS, J. 2016 On the efficiency of gradient based optimization algorithms for DNS-based optimal control in a turbulent channel flow. *Computers & Fluids* **125**, 11–24.
- NOACK, BERND R. 2019 Closed-loop turbulence control-from human to machine learning (and retour). In *Proceedings of the 4th Symposium on Fluid Structure-Sound Interactions and Control (FSSIC)* (ed. Zhou, Y., Kimura, M., Peng, G. Lucey, A.D., Huang & L.), pp. 23–32. Springer.
- NOACK, BERND R., AFANASIEV, KONSTANTIN, MORZYŃSKI, MAREK, TADMOR, GILEAD & THIELE, FRANK 2003 A hierarchy of low-dimensional models for the transient and post-transient cylinder wake. *Journal of Fluid Mechanics* **497**, 335–363.
- NOACK, B. R., CORNEJO MACEDA, G.Y. & LUSSEYRAN, F. 2022 *Machine Learning for Turbulence Control*. Cambridge University Press.
- NOVATI, GUIDO & KOUMOUTSAKOS, PETROS 2019 Remember and forget for experience replay. In *Proceedings of the 36th International Conference on Machine Learning*.
- NOVATI, GUIDO, MAHADEVAN, L. & KOUMOUTSAKOS, PETROS 2019 Controlled gliding and perching through deep-reinforcement-learning. *Phys. Rev. Fluids* **4** (9).
- NOVATI, GUIDO, VERMA, SIDDHARTHA, ALEXEEV, DMITRY, ROSSINELLI, DIEGO, VAN REES, WIM M & KOUMOUTSAKOS, PETROS 2017 Synchronisation through learning for two self-propelled swimmers. *Bioinspir. Biomim.* **12** (3), 036001.
- PAGE, JACOB & KERSWELL, RICH R. 2018 Koopman analysis of burgers equation. *Physical Review Fluids* **3** (7).
- PARK, D. S., LADD, D. M. & HENDRICKS, E. W. 1994 Feedback control of von kármán vortex shedding behind a circular cylinder at low reynolds numbers. *Physics of Fluids* **6** (7), 2390–2405.
- PASTOOR, MARK, HENNING, LARS, NOACK, BERND R., KING, RUDIBERT & TADMOR, GILED 2008 Feedback shear layer control for bluff body drag reduction. *Journal of Fluid Mechanics* **608**, 161–196.
- PEDREGOSA, F., VAROQUAUX, G., GRAMFORT, A., MICHEL, V., THIRION, B., GRISEL, O., BLONDEL, M., PRETTENHOFER, P., WEISS, R., DUBOURG, V., VANDERPLAS, J., PASSOS, A., COURNAPEAU, D., BRUCHER, M., PERROT, M. & DUCHESNAY, E. 2011 Scikit-learn: Machine learning in Python. *Journal of Machine Learning Research* **12**, 2825–2830.
- PIVOT, CHARLES, CORDIER, LAURENT & MATHÉLIN, LIONEL 2017 A continuous reinforcement learning strategy for closed-loop control in fluid dynamics. In *35th AIAA Applied Aerodynamics Conference*. American Institute of Aeronautics and Astronautics.
- POWELL, MICHAEL JD 2006 The newuoa software for unconstrained optimization without derivatives. In *Large-scale nonlinear optimization*, pp. 255–297. Springer.
- PROCTOR, JOSHUA L., BRUNTON, STEVEN L. & KUTZ, J. NATHAN 2016 Dynamic mode decomposition with control. *SIAM Journal on Applied Dynamical Systems* **15** (1), 142–161.
- RABAULT, JEAN, KUCHTA, MIROSLAV, JENSEN, ATLE, RÉGLADE, ULYSSE & CERARDI, NICOLAS 2019 Artificial neural networks trained through deep reinforcement learning discover control strategies for active flow control. *Journal of fluid mechanics* **865**, 281–302.
- RABAULT, JEAN & KUHNLE, ALEXANDER 2019 Accelerating deep reinforcement learning strategies of flow control through a multi-environment approach. *Physics of Fluids* **31** (9), 094105.
- RABAULT, J. & KUHNLE, A. 2022 *Deep Reinforcement Learning applied to Active Flow Control*. Cambridge University Press.
- RABAULT, JEAN, REN, FENG, ZHANG, WEI, TANG, HUI & XU, HUI 2020 Deep reinforcement learning in fluid mechanics: A promising method for both active flow control and shape optimization. *Journal of Hydrodynamics* **32** (2), 234–246.

- RAO, ANIL V 2009 A survey of numerical methods for optimal control. *Adv Astronaut Sci.* **135** (1), 497–528.
- RASMUSSEN, CARL EDWARD 2003 Gaussian processes in machine learning. In *Summer school on machine learning*, pp. 63–71. Springer.
- RASMUSSEN, CARL EDWARD & WILLIAMS, CHRISTOPHER K. I. 2005 *Gaussian Processes for Machine Learning*. MIT Press Ltd.
- RECHT, BENJAMIN 2019 A tour of reinforcement learning: The view from continuous control **2** (1), 253–279.
- REN, FENG, RABAULT, JEAN & TANG, HUI 2021 Applying deep reinforcement learning to active flow control in weakly turbulent conditions. *Physics of Fluids* **33** (3), 037121.
- ROWLEY, C. W. 2005 Model reduction for fluids, using balanced proper orthogonal decomposition. *International Journal of Bifurcation and Chaos* **15** (03), 997–1013.
- SCHÄFER, MICHAEL, TUREK, STEFAN, DURST, FRANZ, KRAUSE, EGON & RANNACHER, ROLF 1996 Benchmark computations of laminar flow around a cylinder. In *Flow simulation with high-performance computers II*, pp. 547–566. Springer.
- SCHAUL, TOM, QUAN, JOHN, ANTONOGLU, IOANNIS & SILVER, DAVID 2018 Prioritized experience replay , arXiv: <http://arxiv.org/abs/1511.05952v4>.
- SCHLICHTING (DECEASED), HERMANN & GERSTEN, KLAUS 2017 *Boundary–Layer Control (Suction/Blowing)*, pp. 291–320. Berlin, Heidelberg: Springer Berlin Heidelberg.
- SCHULMAN, JOHN, WOLSKI, FILIP, DHARIWAL, PRAFULLA, RADFORD, ALEC & KLIMOV, OLEG 2017 Proximal policy optimization algorithms , arXiv: <http://arxiv.org/abs/1707.06347v2>.
- SEIDEL, J, SIEGEL, S, FAGLEY, C, COHEN, K & MCLAUGHLIN, T 2008 Feedback control of a circular cylinder wake. *Proceedings of the Institution of Mechanical Engineers, Part G: Journal of Aerospace Engineering* **223** (4), 379–392.
- SILVER, DAVID, HUANG, AJA, MADDISON, CHRIS J., GUEZ, ARTHUR, SIFRE, LAURENT, VAN DEN DRIESSCHE, GEORGE, SCHRITTWIESER, JULIAN, ANTONOGLU, IOANNIS, PANNEERSHELVAM, VEDA, LANCTOT, MARC, DIELEMAN, SANDER, GREWE, DOMINIK, NHAM, JOHN, KALCHBRENNER, NAL, SUTSKEVER, ILYA, LILLICRAP, TIMOTHY, LEACH, MADELEINE, KAVUKCUOGLU, KORAY, GRAEPEL, THORE & HASSABIS, DEMIS 2016 Mastering the game of go with deep neural networks and tree search. *Nature* **529** (7587), 484–489.
- SILVER, DAVID, HUBERT, THOMAS, SCHRITTWIESER, JULIAN, ANTONOGLU, IOANNIS, LAI, MATTHEW, GUEZ, ARTHUR, LANCTOT, MARC, SIFRE, LAURENT, KUMARAN, DHARSHAN, GRAEPEL, THORE, LILLICRAP, TIMOTHY, SIMONYAN, KAREN & HASSABIS, DEMIS 2018 A general reinforcement learning algorithm that masters chess, shogi, and go through self-play. *Science* **362** (6419), 1140–1144.
- SILVER, DAVID, LEVER, GUY, HEESS, NICOLAS, DEGRIS, THOMAS, WIERSTRA, DAAN & RIEDMILLER, MARTIN 2014 Deterministic policy gradient algorithms. In *Proceedings of the 31st International Conference on International Conference on Machine Learning - Volume 32*, p. 1–387–I–395. JMLR.org.
- SIPP, DENIS & SCHMID, PETER J. 2016 Linear closed-loop control of fluid instabilities and noise-induced perturbations: A review of approaches and tools. *Applied Mechanics Reviews* **68** (2).
- STENGEL, ROBERT F 1994 *Optimal control and estimation*. Courier Corporation.
- SUN, SHILIANG, CAO, ZEHUI, ZHU, HAN & ZHAO, JING 2019 A survey of optimization methods from a machine learning perspective , arXiv: <http://arxiv.org/abs/1906.06821v2>.
- SUTTON, R.S., BARTON, A.G. & WILLIAMS, R.J. 1992 Reinforcement learning is direct adaptive optimal control **12** (2), 19–22.
- SUTTON, RICHARD S & BARTO, ANDREW G 2018 *Reinforcement learning: An introduction*. MIT press.
- SZITA, ISTVÁN 2012 Reinforcement learning in games. In *Adaptation, Learning, and Optimization*, pp. 539–577. Springer Berlin Heidelberg.
- TANG, HONGWEI, RABAULT, JEAN, KUHNLE, ALEXANDER, WANG, YAN & WANG, TONGGUANG 2020 Robust active flow control over a range of Reynolds numbers using an artificial neural network trained through deep reinforcement learning. *Physics of Fluids* **32** (5), 053605, arXiv: 2004.12417.
- UHLENBECK, G. E. & ORNSTEIN, L. S. 1930 On the theory of the brownian motion. *Physical Review* **36** (5), 823–841.
- VANNESCHI, LEONARDO & POLI, RICCARDO 2012 *Genetic Programming — Introduction, Applications, Theory and Open Issues*, pp. 709–739. Berlin, Heidelberg: Springer Berlin Heidelberg.
- VERMA, SIDDHARTHA, NOVATI, GUIDO & KOUMOUTSAKOS, PETROS 2018 Efficient collective swimming by harnessing vortices through deep reinforcement learning. *Proceedings of the National Academy of Sciences* **115** (23), 5849–5854.

- VINUESA, RICARDO, LEHMKUHL, ORIOL, LOZANO-DURÁN, ADRIAN & RABAUULT, JEAN 2022 Flow control in wings and discovery of novel approaches via deep reinforcement learning. *Fluids* **7** (2).
- VLADIMIR CHERKASSKY, FILIP M. MULIER 2008 *Learning from Data*. John Wiley & Sons.
- WANG, JINJUN & FENG, LIHAO 2018 *Flow Control Techniques and Applications*. Cambridge University Press.
- WIENER, N. 1948 *Cybernetics: or the Control and Communication in the Animal and the Machine*. MIT Press, Boston.
- WILLIAMS, RONALD J. 1992 Simple statistical gradient-following algorithms for connectionist reinforcement learning. *Machine Learning* **8** (3-4), 229–256.
- ZHANG, HONG-QUAN, FEY, UWE, NOACK, BERND R., KÖNIG, MICHAEL & ECKELMANN, HELMUT 1995 On the transition of the cylinder wake. *Physics of Fluids* **7** (4), 779–794.